Geophysical Journal International

Geophys. J. Int. (2016) **204,** 1531–1549
GJI Seismology

doi: 10.1093/gji/ggv536

Shear wave splitting of the 2009 L'Aquila seismic sequence: fluid saturated microcracks and crustal fractures in the Abruzzi region (Central Apennines, Italy)

P. Baccheschi,[1] M. Pastori,[2] L. Margheriti[2] and D. Piccinini[3]

[1]*Istituto Nazionale di Geofisica e Vulcanologia, Via dell'Arcivescovado* 8, *I*-67100 *L'Aquila, Italy. E-mail: paola.baccheschi@ingv.it*
[2]*Istituto Nazionale di Geofisica e Vulcanologia, Via di Vigna Murata* 605, *I*-00143 *Rome, Italy*
[3]*Istituto Nazionale di Geofisica e Vulcanologia, Via della Faggiola* 32, *I*-56126 *Pisa, Italy*

Accepted 2015 December 14. Received 2015 December 12; in original form 2015 May 13

SUMMARY

The Abruzzi region is located in the Central Apennines Neogene fold-and-thrust belt and has one of the highest seismogenic potential in Italy, with high and diffuse crustal seismicity related to NE–SW oriented extension. In this study, we investigate the detailed spatial variation in shear wave splitting providing high-resolution anisotropic structure beneath the L'Aquila region. To accomplish this, we performed a systematic analysis of crustal anisotropic parameters: fast polarization direction (φ) and delay time (δt). We benefit from the dense coverage of seismic stations operating in the area and from a catalogue of several accurate earthquake locations of the 2009 L'Aquila seismic sequence, related to the M_w 6.1 2009 L'Aquila main shock, to describe in detail the geometry of the anisotropic volume around the active faults that ruptured. The spatial variations both in φ and δt suggest a complex anisotropic structure beneath the region caused by a combination of both structural- and stress-induced mechanisms. The average φ is NNW–SSE oriented (N141°), showing clear similarity both with the local fault strike and the SH_{max}. In the central part of the study area fast axes are oriented NW–SE, while moving towards the northeastern and northwestern sectors the fast directions clearly diverge from the general trend of NW–SE and rotate accordingly to the local fault strikes. The above-mentioned fault-parallel φ distribution suggests that the observed anisotropy is mostly controlled by the local fault-related structure. Toward the southeast fast directions become orthogonal both to strike of the local mapped faults and to the SH_{max}. Here, φ are predominantly oriented NE–SW; we interpret this orientation as due to the presence of a highly fractured and overpressurized rock volume which should be responsible of the 90° flips in φ and the increase in δt. Another possible mechanism for NE–SW orientation of φ in the southeastern sector could be ascribed to the presence of a buried, deep NE–SW oriented fault system. δt, both unnormalized and normalized, does not show any clear evidence of increasing with increasing depth indicating that the anisotropy is confined primarily to the shallower crustal layers (∼10 km depth). Interpolating δt show that higher values are found at the edges of the main patches of the rupture related to the 2009 main shock, while lower values are limited in the central part of the fault plane, where the coseismic slip was higher. We infer that in the areas surrounding the ruptured region, lateral variations in material properties caused overpressurized fluid conditions, while within the main shock ruptured area, high energy released produced an open crack system such that overpressurization was not possible.

Key words: Seismic anisotropy; Wave propagation; Fractures and faults; Crustal structure.

1 INTRODUCTION

Seismic anisotropy is a common property of the Earth's crust. In recent years, there have been a growing number of studies that recognized anisotropy in many different geological and structural domains (Crampin & Lovell 1991; Tadokoro *et al*. 1999; Peng & Ben-Zion 2004, 2005; Mizuno *et al*. 2005).

The most common method for recognizing seismic anisotropy is the 'Shear Wave Splitting' technique. When a seismic wave enters an anisotropic medium it splits into two orthogonally

polarized components, namely fast and slow components, which travel with different velocities as a function of their propagation and polarization directions. The time lag between the *S*-fast and *S*-slow component is the delay time (δt), which is a measure of the intensity and/or the depth extension of the anisotropic layer. When the observed delay time is close to zero the measure is called 'null' and it means that shear wave splitting did not occur. This can be due to the absence of anisotropic structure beneath the station, but it can also mean that the shear wave is initially polarized parallel to either the fast or slow direction (Schutt *et al*. 1998). In this case, the original seismogram shows a linearly polarized *S* wave.

The model that is widely hypothesized to explain the majority of observed crustal anisotropy is the stress-induced anisotropy (Nur & Simmons 1969), known as extensive dilatancy anisotropy (EDA) model (Crampin 1978; Crampin & Peacock 2005). In this model, the shear wave splitting is caused by stress-aligned fluid-saturated parallel, near vertical microcracks and pore throats or by preferential closure of fractures in rock by the *in situ* stress field (Boness & Zoback 2004). The microcracks (EDA cracks) are aligned by the regional stress field parallel to SH_{max}, the direction of horizontal maximum active compressive stress (Crampin & Lovell 1991) and, for nearly vertical propagation of seismic waves, shear waves are generally polarized so that the fast components are parallel to the strike of EDA cracks and fractures. Consequently, fast polarization directions are aligned parallel to the SH_{max}. The delay time is a measure of the intensity of the anisotropy, which in this case corresponds to crack density and/or the thickness of the fracture field (Crampin 1994).

In some cases, the EDA model cannot explain the pattern of fast directions. This is observed when the fast components are aligned parallel to the structural fabric (Kaneshima 1990; Gledhill 1991), as predicted by the structural-controlled anisotropy model (SAM; Zinke & Zoback 2000). The SAM model describes such a pattern of fast directions. In this model, the seismic anisotropy is controlled by the intrinsic structural fabric of the rocks and is not necessarily related to the active stress field. The shear wave splitting arises from the preferential alignment of macroscopic structural features such as finely layered sedimentary sequences (Backus 1962; Kern & Wenk 1990; Leary *et al*. 1990), pervasive fault-zone fabric (Zhang & Schwartz 1994; Tadokoro *et al*. 2002), macroscopic aligned fractures (Mueller 1991; Zinke & Zoback 2000), oriented anisotropic minerals giving rise to the foliation in metamorphic rocks (Brocher & Christensen 1990; Aster & Shearer 1992; Sayers 1994; Valcke *et al*. 2006; Kendall *et al*. 2007) and alignment of grains (Balfour *et al*. 2005; Verdon *et al*. 2008). In this model, the delay time measures the degree of fabric strength (Savage *et al*. 1990).

The aim of this paper is to provide new insights in the anisotropic properties of the L'Aquila area, which has been struck by a destructive M_w 6.1 earthquake on 2009 April 6, at 01:32 UTC (Scognamiglio *et al*. 2010). Starting from the previous anisotropic study available for the area (Pastori *et al*. 2012), we further investigated these issues taking advantage of the dense coverage of temporary and permanent seismic stations operating in the area soon after the occurrence of the main shock. The increased number of seismic stations and the catalogue of accurate earthquake locations allowed us to collect thousands new splitting measurements, which enabled us to better understand the causes of anisotropy and its variations in space.

1.1 Seismotectonics of the area

The study area is located in the axial portion of the Central Apennines fold-and-thrust belt formed during the Neogene-Quaternary times as a response to the synchronous opening of the Tyrrhenian backarc basin, the eastward rollback of the subducting Adria lithosphere and the eastward migration of the Apenninic compressional front (Fig. 1; Malinverno & Ryan 1986; Rosenbaum *et al*. 2002). The present-day structural setting of the L'Aquila area is the result of several overthrust tectonic units belonging to the transitional domain between the Latium–Abruzzi carbonate shelf platform and the Umbria–Marche pelagic basin. These two domains were separated by the Olevano-Antrodoco tectonic Line (OAL), which developed during the Liassic extension stage (Fig. 1; Castellarin *et al*. 1982; Calamita & Deiana 1988; Bigi & Pisani 2005): northwest of the OAL is the Umbria-Marche pelagic domain, southeast of the OAL is the Latium-Abruzzi carbonate shelf platform.

Since the Early Pleistocene the central sector of the Apenninic chain was affected by an NE-striking extensional tectonic regime acting on an area previously controlled by compressive tectonics (Barchi *et al*. 2000; Galadini & Galli 2000; Boncio *et al*. 2004). The NE-oriented extension regime affects the axial and inner portions of the belt, while compressive structures characterized the external foredeep areas (Montone *et al*. 2012). At present, the NE–SW active extension (Sh_{min}) in the Central Apennines accommodates ∼3 mm yr^{-1} extension rate across the belt (D'Agostino *et al*. 2008; Cheloni *et al*. 2014). The extension is controlled by a complex and broad system of active NW–SE striking normal faults, which reactivate pre-existing compressional structures (Patacca *et al*. 2008; Pizzi & Galadini 2009). Two dominant subparallel fault sets, namely the Eastern Normal Fault System (ENFS) and the Western Normal Fault System (WNFS), are composed of adjacent, mostly SW-dipping and *en-échelon* arranged fault segments (Vezzani & Ghisetti 1998; Barchi *et al*. 2000; Roberts & Michetti 2004). These normal faults controlled the formation of large intermountain extensional basins, such as the L'Aquila basin, interposed between the two previously major fault systems. The L'Aquila region is an NW–SE elongated continental basin filled by Plio-Quaternary continental sediments (Cavinato & De Cellis 1999; Galadini & Galli 2000). It is located within the Middle Aterno Valley basin, a northwest–southeast-trending tectonic depression located between the Gran Sasso Thrust and the Monti d'Ocre morphostructural units (Fig. 1; Bagnaia *et al*. 1992; Blumetti *et al*. 2002; Boncio *et al*. 2004; Blumetti & Guerrieri 2007; Civico *et al*. 2015a).

1.2 The 2009 L'Aquila seismic sequence

In 2009, a destructive seismic sequence hit central Italy destroying the L'Aquila town and the surrounding villages (Fig. 1). The spatiotemporal evolution of the seismic sequence and the geometry of the fault system responsible for the sequence have been accurately reconstructed in the last years by several authors (Chiarabba *et al*. 2009; Valoroso *et al*. 2013, and references therein) taking advantage of thousands of aftershocks recorded at several seismic stations. The sequence occurred in the region located between the WNFS and the ENFS major subparallel normal fault systems and is characterized by a long sequence of foreshocks and aftershocks. The foreshock sequence started on 2009 January, the two largest foreshocks were the M_w 4.1 on March 30 (at 13:38 UTC) and the M_w 3.9 on April 5 (at 20:48 UTC). The M_w 6.1 main shock struck

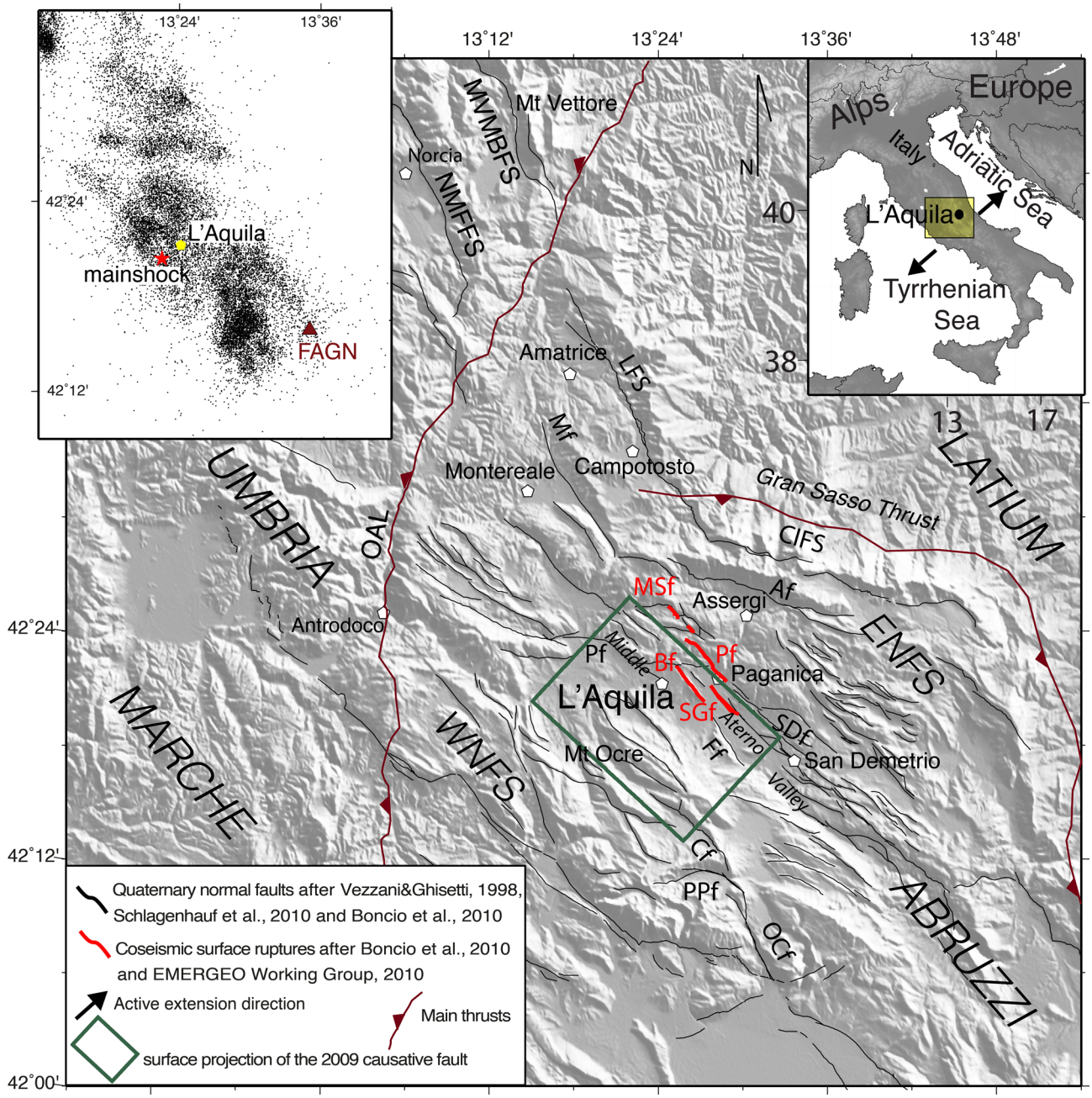

Figure 1. Schematic tectonic map of Abruzzi region with the traces of the Quaternary active normal faults (black lines) according to various authors reported in the lower left inset. The main faults are labeled as follows: NMFFS: Norcia-Mt. Fema fault systems; MVMBFS: Mt. Vettore–Mt. Bove fault systems; LFS: Mt. della Laga fault system; Mf: Montereale fault; Af: Assergi fault; CIFS: Campo Imperatore fault system; Pf: Pettino fault; SDf: San Demetrio fault; Ff: Fossa fault; PPf: Piano di Pezza fault; OCf: Ovindoli-Celano fault; Cf: Campo Felice fault. The red traces are the coseismic surface ruptures (modified after: Boncio *et al*. 2010; EMERGEO Working Group 2010) labeled as follows: MSf: Mt. Stabiata fault; Pf: Paganica fault; SGf: San Gregorio fault; Bf: Bazzano fault. The dark red lines represent the Olevano-Antrodoco Line (OAL) and the Gran Sasso Thrust. The green box is the approximate surface projection of the 2009 main shock causative fault as modeled by Cirella *et al*. (2012) by joint inversion of strong motion, GSP and DInSAR data. Black arrows in the upper right inset show the direction of the active extension across the Central Apennines (Montone *et al*. 2012). The upper left inset shows the 2009 seismic sequence (from ISIDE: Italian Seismological Instrumental and Parametric Data Base; http://iside.rm.ingv.it/iside/standard/index.jsp). A clear cut-off of earthquake hypocentres is recognized in correspondence of the southeastern termination of the Middle Aterno Valley, where the station FAGN is located.

the area on 2009 April 6 at 01:32 UTC (Scognamiglio *et al*. 2010) and nucleated at ∼8.5 km depth, breaking a 15–18 km long fault segment with patches of slip larger than 0.7 m. The fault plane was associated with the Paganica-San Demetrio fault, a poorly known tectonic structure before 2009 April (Boncio *et al*. 2004), which matches the coseismic surface ruptures mapped by the EMERGEO Working Group (2010) and Boncio *et al*. 2010. This surface fracture was observed soon after the main shock and was interpreted as a direct expression of fault rupture at seismogenic depth. The focal mechanism solution for the main shock shows a pure normal faulting mechanism (Pondrelli *et al*. 2010; Herrmann *et al*. 2011), striking N138° and dipping about 54° towards SW.

The aftershock distribution, whose sequence includes the largest earthquakes M_w 5.6, April 7 (17:47 UTC) located at about 15 km depth and the M_w 5.4, April 9 (00:53 UTC) occurred at about 9 km depth, allows the delineation of a complex NW-trending extensional fault system of about 50 km long. The large number of aftershocks along with the occurrence of moderately sized earthquakes provided enough data for estimating the stress field. Most of the aftershock focal mechanisms show a predominant NW–SE striking focal plane, which is coherent with the strike of the faults mapped in the region (Scognamiglio *et al*. 2010; D'Amico *et al*. 2013). Pondrelli *et al*. (2010) show a predominant *T*-axes orientation N60° in the north and central sectors of the Abruzzi region, while moving towards the southern sector, the *T*-axes orientation varies between N020° and N070°. The results of the stress tensor inversion obtained using the focal solution indicate homogeneous stress distribution with subhorizontal $\sigma 3$ trending N232° confirming an extensional stress regime. These results are in agreement with the present-day NE-trending horizontal extension (Montone *et al*. 2012).

1.3 Anisotropy in the crust

The close correlation between the direction of the fast shear wave, the SH_{max} direction and the dominant fracture orientation make seismic anisotropy a powerful tool to characterize the deformation associated with a wide range of tectonic processes as well as the fault zone fabric (Crampin & Gao 2008). In addition, it should be an indicator of the presence of fluid-saturated cracks in rock volumes (Zhang & Schwartz 1994; Crampin & Chastin 2003; Mizuno *et al*. 2005; Liu *et al*. 2008; Balfour *et al*. 2012).

A large number of studies show a sharp coherence between the leading polarization direction and the maximum horizontal compressive stress SH_{max}, implying that the EDA cracks are the primary causes of shear wave splitting (Margheriti *et al*. 2006; Gao & Crampin 2008; Martin *et al*. 2014; Frietsch *et al*. 2015). Stress-induced anisotropy has been suggested to explain the pattern of seismic anisotropy in the central Japan (Hiramatsu *et al*. 2010) and in the forearc of the Northern Cascadia subduction zone (Balfour *et al*. 2012). On the other hand, SAM has been suggested for the Karadere–Düzce branch of the North Anatolian Fault (Li *et al*. 2014), for the Eastern Betic Cordillera, Spain (Buontempo & Wuestefeld 2013), around the Gulf of Corinth, Greece (Bouin *et al*. 1996), the Atotsugawa Fault, Japan (Mizuno *et al*. 2005) and in Northern Cascadia (Matharu *et al*. 2014). Moreover, the anisotropic properties within the fault zone and the surrounding rock volume might often result from the mixture of both structural and stress-induced mechanisms. In this case, it is quite difficult to discriminate which of the two mechanisms is responsible of the observed anisotropy. The most common situation is a combination of stress-aligned microcracks away from the fault and shear fabric controlled anisotropy close to the damage zone, as observed around the San Andreas Fault (Zhang & Schwartz 1994; Boness & Zoback, 2004, 2006; Cochran *et al*. 2006) near the Calaveras Fault, California (Zinke & Zoback 2000), near Parkfield, California (Liu *et al*. 1997, 2008), in Northwest Turkey (Hurd & Bohnhoff 2012; Eken *et al*. 2013), around the Greendale Fault, New Zealand (Syracuse *et al*. 2012). In the Italian Peninsula, stress-induced anisotropy has been suggested to explain the anisotropic structure in the Reggio Emilia region (Margheriti *et al*. 2006), in the Umbria-Marche region (Piccinini *et al*. 2006), in the L'Aquila surrounding (Pastori *et al*. 2012) and beneath the Val d'Agri basin (Pastori *et al*. 2009). For the cases in the Italian Peninsula, the contribution from structural-related anisotropy cannot be completely ruled out because of the sharp coherence between the leading polarization direction and the strike of active faults affecting the areas.

1.4 Previous studies of anisotropy in the region

Previous studies of seismic anisotropy in the L'Aquila surroundings showed that the majority of fast directions are consistent both with the strike of the main active faults and with the SH_{max}, which, in regions undergoing extension, coincide. Pastori *et al*. (2012) analysed the *S*-splitting from earthquakes recorded throughout 2009 at three permanent stations. The obtained results show a predominant fast direction WNW–ESE-oriented (about N122°), which is parallel to the strike of the active faults as well as the SH_{max} orientation. These authors interpreted the observed anisotropy primarily in terms of stress-aligned fluid-filled microcracks, as suggested by the EDA model. The sharp coherence between the fast direction and the strike of major faults bounding the basin allows these authors to not completely rule out the contribution due to the inherited structural fabric, as proposed by Zinke & Zoback (2000) model. In another study, Lucente *et al*. (2010) investigate the role played by the high pore-fluid pressure analysing the spatiotemporal variations of v_p/v_s ratio and of the anisotropic parameters during the foreshock sequence at the seismic station AQU located in L'Aquila town and found an abrupt change in the elastic parameters, just before the main shock occurrence. Such changes suggest to these authors to consider a sequence of dilatancy and fluid-diffusion processes in the rock volume surrounding the nucleation area, which is possibly responsible for the 90° flips of the fast directions in some of the events that occurred in the days around the main shock at AQU station. Similarly, 90° flips in polarization due to fluid overpressure has also been suggested by Pastori *et al*. (2012) to explain the rotation of fast directions at the station FAGN, located SE of the main shock. At this site, the average fast direction shows a predominantly SSW–NNE strike (about N28°), thus becoming perpendicular to the SH_{max} and to the fast polarization directions observed at the other stations in the area. Pastori *et al*. (2012) interpreted this rotation as likely due to the overpressurized fluids in some pockets at the fault rupture edge, hypothesizing that fluids are of primary importance in the 2009 L'Aquila seismic sequence as also conceived by Terakawa *et al*. (2013).

2 DATA AND ANALYSIS METHOD

Our data set consists of three-component waveforms, sampled at 125 sps. The three-component seismograms were recorded at 55 stations, belonging to two permanent and two temporary seismic deployments (Fig. 2). The permanent network consists of four digital broad-band stations (AQU, CAMP, FAGN, FIAM), which is part of the Seismic National Network managed by the Istituto Nazionale di Geofisica e Vulcanologia of Rome (INGV). We benefit from data recorded at two stations (PRE1 and MTR2) of the permanent regional seismic network managed by the INGV personnel based in L'Aquila town.

Soon after the April 6 main shock, to better capture the seismic sequence, two temporary deployments were installed within the epicentral area. The first consisted of 33 INGV temporary broad-band seismic stations (RM01, RM02, . . . RM33) operating until the end of 2009 December. The second network consisted of 20 portable broadband seismometers (LG01, LG02, . . . LG20) operating from 2009 May to July installed by the Laboratoire de Géophysique

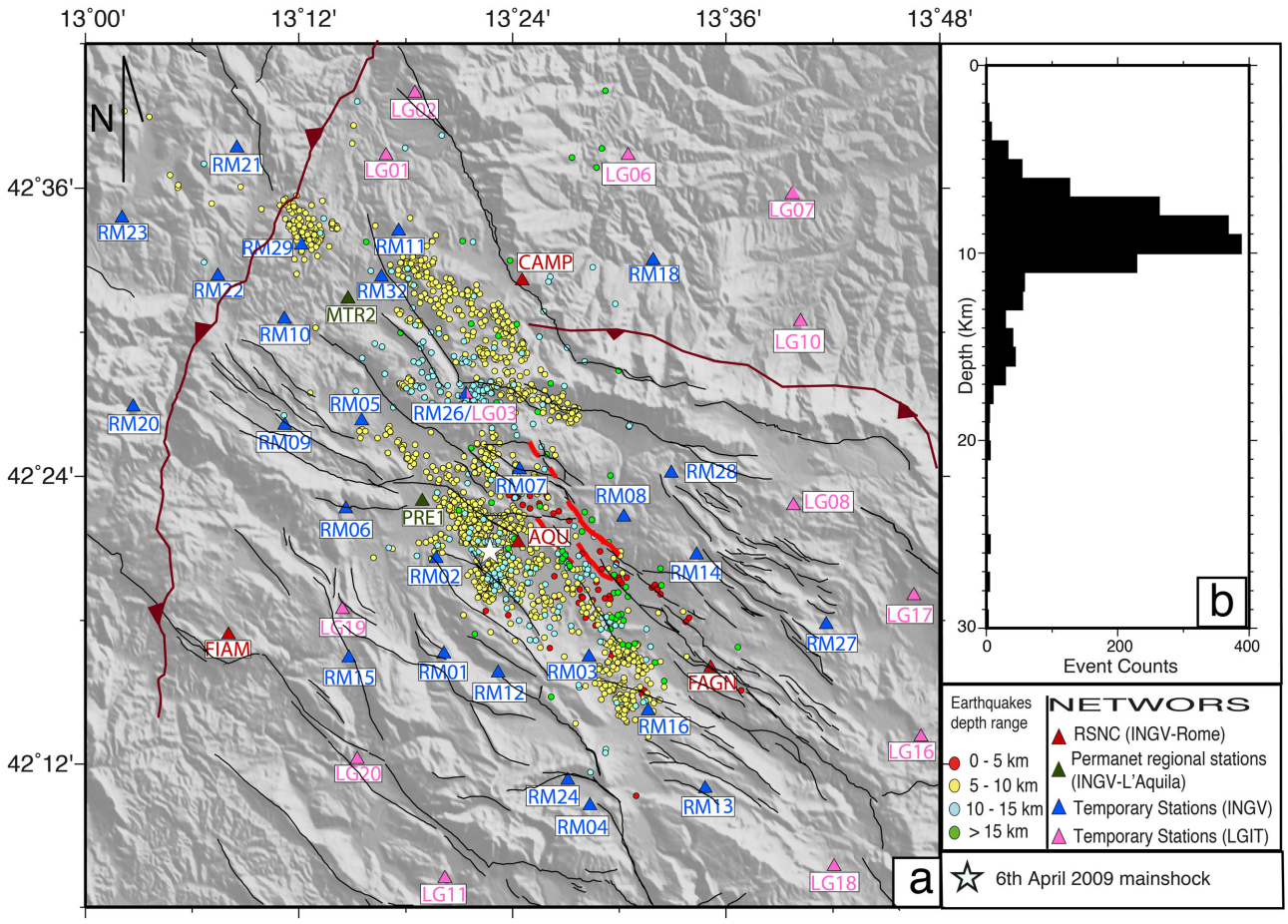

Figure 2. (a) Map of the hypocentral distribution of the well-located 3600 events used in this study and recorded during the 2009 seismic sequence (Chiaraluce *et al*. 2011). The events are coloured as a function of depth. Stations used for splitting analysis are symbolized with triangles; red and green triangles are the permanent national and regional stations, respectively; the blue and magenta triangles are the INGV and LGIT temporary stations, respectively, installed soon after the 2009 April 6 main shock. The AQU station is in L'Aquila town. (b) Histogram showing the depth distribution of the seismicity: most of hypocentres are confined between 8 and 12 km depth.

Interne et Tectonophysique of Grenoble. After 2009 June, the station LG03 was replaced by the station RM26 (Margheriti *et al*. 2010). We therefore discuss the results considering them as one station (RM26/LG03).

For our analysis, we used a catalogue of 3600 well-located earthquakes with a magnitude range between 1.9 and 6.1 for foreshock and aftershock sequences (Chiaraluce *et al*. 2011). Only earthquakes recorded during 2009 have been analysed in this study. The hypocentres are primarily confined within the upper 12 km, with the exception of April 7 aftershocks located at depth of 15 km, even if deeper seismicity, up to 20 km depth, has also been located.

Due to the large amount of earthquakes to be processed, we used the automated code *ANISOMAT+* (Piccinini *et al*. 2013) to estimate the anisotropic parameters, φ and δt. The code is automated and this guarantees an unbiased assessment of the *S*-wave splitting parameters. The code is based on the cross-correlation (CC) method (Bowman & Ando 1987) assuming that the *S*-fast and *S*-slow horizontal components have similar waveforms. The two horizontal seismograms (the NS and EW components) are rotated in the horizontal plane by 1° of increment of azimuth from 0° to 180°. For each azimuth, the CC coefficient between the two horizontal seismograms is calculated for a range of times delay in a selected time window. The azimuth for which the maximum absolute value of CC coefficient is reached represents the polarization direction φ and the corresponding value of time lag is the delay time δt between the *S*-fast and *S*-slow components (for the complete description of the code and how it works the reader is referred to Piccinini *et al*. 2013).

Fig. 3 shows an example of analysis for the 2009 March 26 06:13:27 event observed at AQU station, which is one of the stations that recorded the greatest number of events.

To accomplish a reliable estimate of the splitting parameters, from the whole data set we selected only those waveforms that satisfy these criteria, following the approach used by Peng & Ben-Zion (2004):

(1) Seismic rays having a geometrical incidence angle $i_c \leq 45°$. This criterion allowed us to select waveforms coming from earthquakes close to the stations. This means that the analysis was performed only on *S* waves recorded within the shear wave window. The latter is defined by incidence angle at the free surface less than the critical angle, $i_c = \sin^{-1}(Vs/Vp)$, where *Vp* and *Vs* are the *P*- and *S*-wave velocities, respectively (Booth & Crampin 1985). This restriction guarantees that the *S* waves do not interact with any free surface or horizontal interface, keeping the particle motion out from complication deriving from *S* to *P* converted phases (Booth & Crampin 1985), free surface effects (Nuttli 1961) and phase changes at crustal discontinuities (Liu & Crampin 1990);

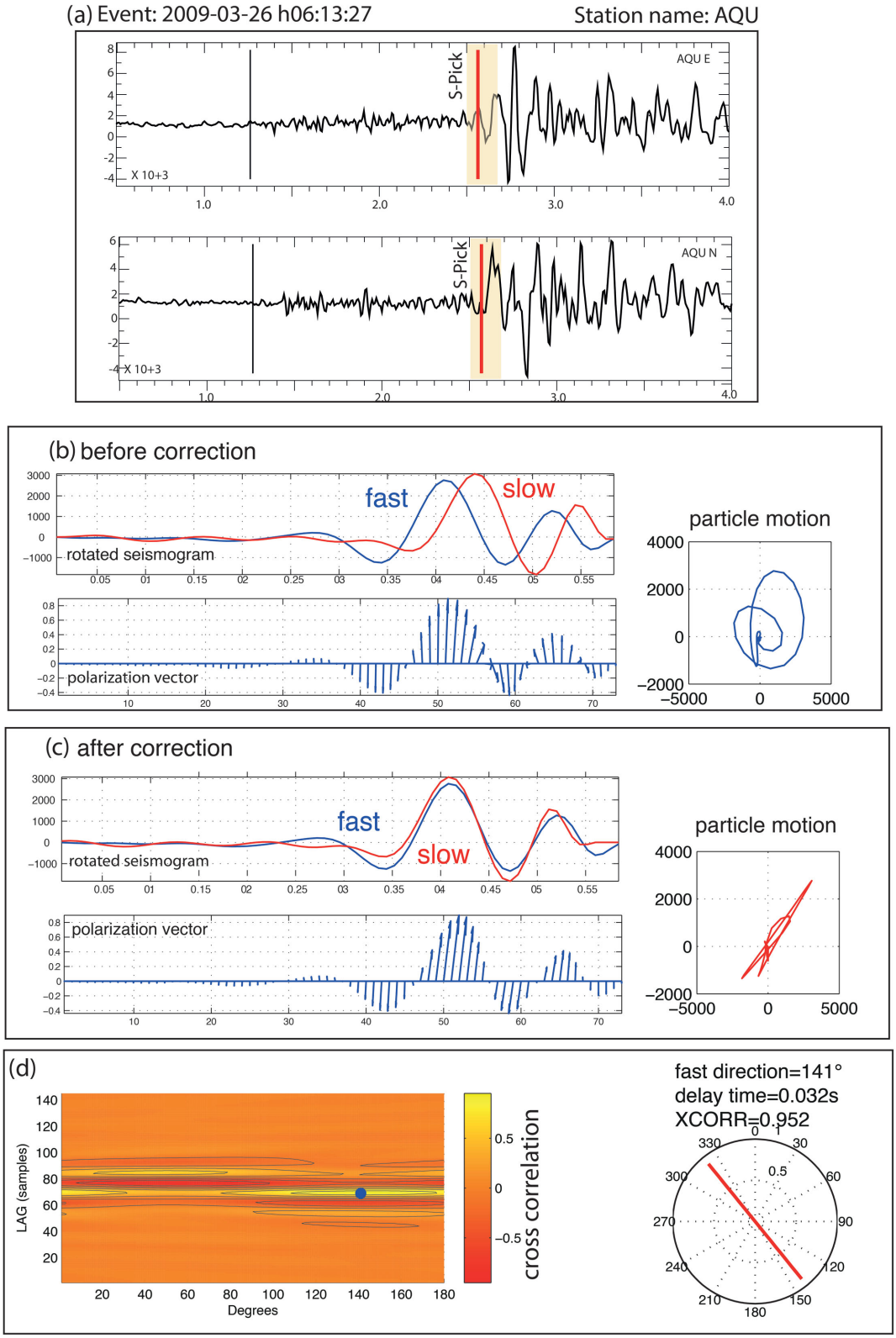

Figure 3. Example of a well-constrained splitting measurement for the 2009 March 26 06:13:27 event at AQU station obtained by using ANISOMAT+ code (Piccinini *et al*. 2013). The upper panel (a) shows the S picking on the N–S and E–W components. The time window used for splitting analysis is highlighted in yellow. The middle panels show the rotated seismograms into fast and slow directions, the polarization vectors and the horizontal particle motions before (b) and after (c) correction. The last panel (d) displays the estimate of cross-correlation value (blue dot), on the left side, and the fast polarization direction, on the right side.

(2) *S*-to-*P* amplitude ratio (calculated as the amplitude of a window starting at the *S*-wave onset divided by the amplitude of a time window containing the *P* wave) > 4.

(3) The amplitude of the horizontal components larger than the corresponding vertical component (H/V ratio). The criteria 2 and 3 let us to reject data with a possible contamination by the *P*-wave coda (high *S*-to-*P* ratio) and to use only waveforms with small *S*-wave amplitude on the vertical component (high H/V).

To improve the signal-to-noise ratio and clearly identify the shear wave signal, prior to the splitting analysis all waveforms have been bandpass filtered at 1–10 Hz using a bandpass Butterworth fourth-order two-pass filter. We applied this filter on the basis of the dominant frequency for local earthquake shear wave, which ranges from 5 to 10 Hz. Afterward, seismograms are windowed around shear wave arrivals. We selected a time window length of about 0.35 s centred on the automatic pick of *S* arrival (Di Stefano *et al*. 2006; Aldersons *et al*. 2009), fixing the start of the windows 0.15 s before the *S* arrival pick.

To guarantee consistency of results we consider only those measurements showing a CC coefficient larger than or equal to 0.7.

The final collection consists of 3732 new individual event-station pair splitting measurements including 'null' measurements. In this study, we considered as 'null' results those measures with a delay time lower or equal to 0.016 s. We also checked the initial polarization directions of these *S* waves to verify if null splittings are related to fast and slow polarization directions (Wüstefeld & Bokelmann 2007).

3 RESULTS

The selection made on the base of the above criteria allowed us to collect 1756 new high-quality splitting measurements at 23 stations. The splitting analysis also yielded 1396 'null' measures. Our results reveal a quite complex pattern of fast directions and magnitude of delay time values (Table S1, Supplementary material), which can be probably attributed to the different properties characterizing the different regions sampled by the seismic rays. The pattern of single measurements (Fig. S1, Supplementary material) does not show a homogeneous trend and it is quite difficult to recognize a preferred orientation of the fast direction. Such a complexity could arise by the changing of the anisotropic properties encountered by the ray while moving through different sectors of the region from hypocentre to the station, resulting in a lateral variation of anisotropy. The delay time values range between 0.024 and 0.26 s. The average value of splitting delay is approximately 0.07 s with standard deviation of 0.036 s. Similar δt values are in agreement with delay times found in other regions, such as Karadere-Düzce Fault (Peng & Ben-Zion 2004) or Izmit region (Hurd & Bohnhoff 2012). The fast directions are variable but the distribution for the whole data set shows a predominant NNW–SSE orientation (N141°) (Fig. 4b).

The rose diagram of the total 'null' directions has two main peaks (Fig. 4b), one with a local maxima approximately parallel to the main fast direction and one perpendicular to it, as expected for the slow direction. Analysing the whole data set, the number of null measurements ($\delta t < 0.016$ s) is about 30 per cent of the total and at single stations the percentage of nulls is quite variable, ranging between 10 and 80 per cent.

In the following paragraphs, we discuss only the results for 23 stations since they recorded more than eight 'non-null' high-quality splitting measurements.

3.1 Spatial distribution of fast directions

In order to analyse the anisotropic results, at each of the selected stations we have evaluated the rose diagram (Fig. 4a). To provide a statistical analysis of the measurements at these stations we first doubled the measured φ and then we applied the Von Mises method to calculate the resultant length R and the mean fast direction $\bar{\varphi}$ with the standard deviation σ (Table S1; Davis 1986; Mardia & Jupp 2000; Cochran *et al*. 2003). For N measurements:

$$S = \sum_{i=1}^{N} \sin(2\varphi_i) \tag{1}$$

$$C = \sum_{i=1}^{N} \cos(2\varphi_i) \tag{2}$$

$$\bar{\varphi} = \tan^{-1}(S/C) \tag{3}$$

$$\bar{R} = \frac{\sqrt{S^2 + C^2}}{N} \tag{4}$$

$$\sigma = \frac{\mathrm{rad}}{2}\sqrt{2x\left(1.0001 - \frac{\sqrt{\sum_{i=1}^{N}\sin(2\varphi_i)^2 + \sum_{i=1}^{N}\cos(2\varphi_i)^2}}{N}\right)} \tag{5}$$

The R-value expresses a quantitative measure of the strength of alignment of the fast directions and varies between 0 and 1, where 0 indicate random orientation and 1 total alignment of data.

Looking at the station rose diagrams (Fig. 4) we note that the majority of stations (FAGN, AQU, RM11, RM26/LG03, RM08, RM07, RM01, RM24, RM02, RM06, RM09, RM10, RM29, LG19 and PRE1) show moderate scattered petals, with R-value between 0.3 and 0.65. Out of the 23 only 4 stations (RM03, RM05, RM14 and RM21) have $R \leq 0.3$, indicating that $\bar{\varphi}$ at these stations are highly scattered. The scatter behaviour of fast directions might be due to the presence of locally complex anisotropy structures or to variation in time of the anisotropic parameters related to stress changes during the seismic sequence.

There are only three stations (CAMP, RM04, RM32) that have R-value ≥ 0.65, indicating that the $\bar{\varphi}$ have a significant preferred direction.

The average fast direction at each station is plotted over the corresponding rose diagrams on the map (Fig. 4a). At first glance, we note three different patterns moving from the northwestern to the southeastern sector of the region: the dominant shear wave polarization varies from N–S to NW–SE and NE–SW. The N–S striking trend of the averaged fast directions is well recognized for those stations located in the northwestern boundary of the study area, and to the most external sector of the right flank of the Middle Aterno Valley (see RM29, RM10, RM09 and LG19): for these stations the mean fast axes are not parallel to the main Quaternary normal faults nor to the regional SH_{max}. Moving towards the internal sector of the right flank of the Middle Aterno Valley, most of the stations show dominant shear wave polarization about NNW–SSE. This trend of φ is parallel both to the strike of nearby Quaternary normal faults in the region and to the regional SH_{max} direction. At stations located on the northeastern boundary of the study area, the mean fast direction rotates from NNW–SSE (at stations CAMP, RM11, RM32) to ENE–WSW (at station RM26/LG03). This rotation of ϕ directions seems to follow the strike of the Gran Sasso Thrust as well as the Campo Imperatore normal fault systems and the Monti della Laga

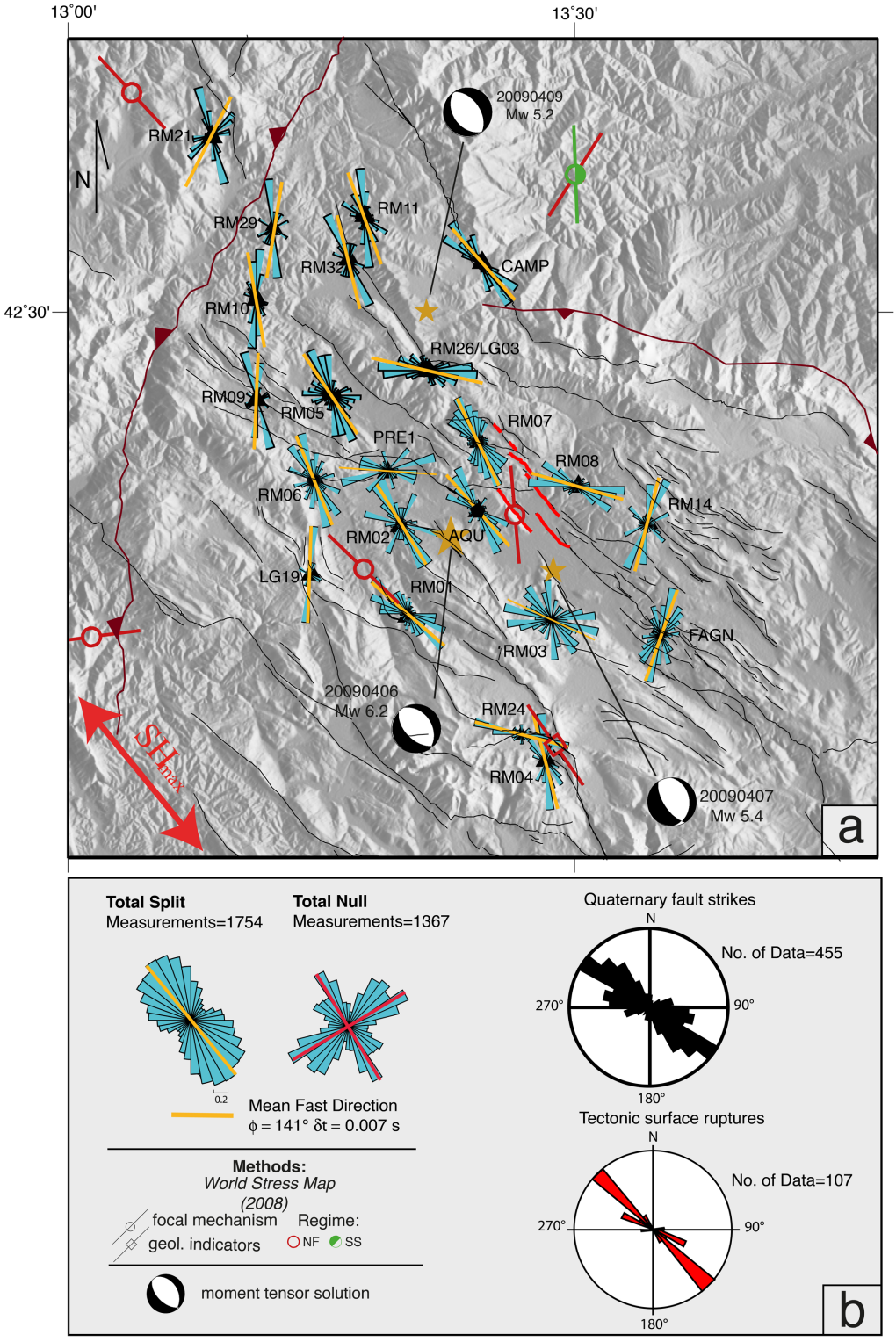

Figure 4. (a) Map of rose diagrams showing the fast polarization directions. The trend of each petal represents the φ direction and the length is proportional to the number of measurements in the same intervals of φ (10°) weighted by the δt of the measurements. The rose diagrams are only shown for stations with ≥8 good splitting measurements. For each station the mean fast direction (orange bar) is also reported. Also are reported the stress indicators available for the study area (World Stress Map website: http://dc-app3-14.gfz-potsdam.de/pub/introduction/introduction_frame.html), the focal mechanisms of the main shock (M_w 6.1, 2009 April 6 at 01:32 UTC) and of the two greatest aftershocks (M_w 5.4, 2009 April 7 at 17:47 UTC; M_w 5.2, 2009 April 9 at 00:52 UTC) (D'Amico *et al*. 2013). (b) Rose diagram and mean fast direction for the whole data set of high-quality splitting results: most of fast directions are about NW–SE (N141°), coherent with the strike of faults and with SH_{max}. This result is in agreement with the frequency distribution of the Quaternary fault strikes and coseismic surface ruptures: both the related rose diagrams show a predominant NW–SE mean strike of the Quaternary faults (modified after Galadini & Pizzi 2009) and of the surface ruptures (modified after EMERGEO Working Group 2010). Rose diagrams for the whole data set of 'null' direction show bimodal distribution (red bars), having one direction parallel to and the other one perpendicular to the mean fast direction, as expected for the slow direction.

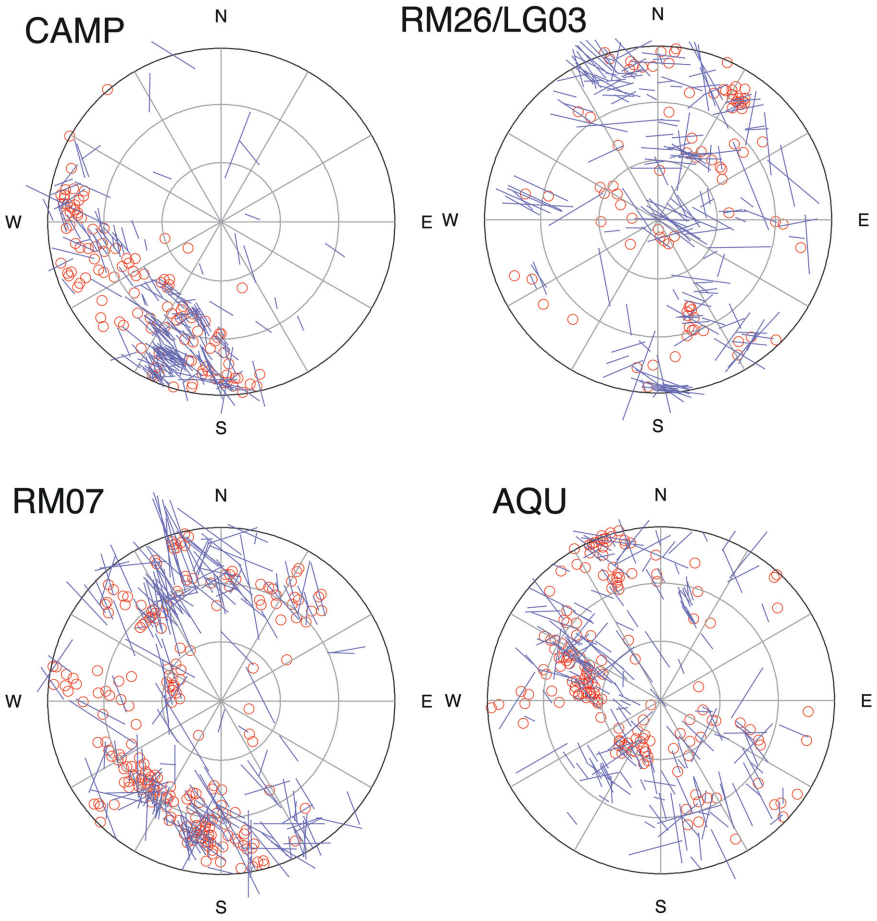

Figure 5. Equal area projection of splitting results plotted with respect to the backazimuth and geometrical incidence angle. For each equal area projection, the circles represent the incidence angle from 0° to 45° in 15° increments. Equal area plots are shown only for those stations with the maximum number of good measurements (blue bars scaled by delay time) and with good azimuthal coverage. For the same stations we have also reported the null measurements (small red open circles). Stations are ordered moving from NW to SE through the study area.

fault systems, and could suggest an important contribution to the anisotropy from the major Quaternary structural lineaments.

A different and interesting pattern of the mean fast direction is found in the southeastern and in the southwestern sector of the study area. In the southeastern sector, stations FAGN and RM14 returned mean fast direction oriented NE–SW, almost perpendicular to the orientations observed at the other stations and to the surface local traces of faults. The station FAGN is installed southeast of the San Demetrio fault and recorded large *S*-wave amplitudes that are interpreted as trapped waves (Calderoni *et al*. 2012). It is possible that trapped waves can modify the *S*-waves seismograms and, thus, cause the 90° flips in orientation. Moving towards the southwestern sectors stations RM04 and RM24 are closely spaced but show different fast direction orientations. The mean fast direction at RM04 is around 165°N, while at RM24 is around 105°N. Similar change in fast direction between closely spaced stations could be attributed to localized and heterogeneous anisotropic structures suggesting that the source of the anisotropy could likely be shallow and very complex. Moreover the mapped faults located in the area show a great complexity, which should explain the strong difference between the observations obtained at the two stations.

The results at each single station are also displayed on equal area projections (Fig. 5). In this type of visualization the fast directions are plotted with respect to backazimuth and incidence angle; this should help to better recognize possible spatial variations of shear wave splitting. Fig. 5 shows the four stations with better azimuthal coverage; the plots related to the other stations are in the supplementary material (Fig. S2a,b).

At stations AQU, RM07, RM26/LG03 and CAMP we can identify patterns in the anisotropic parameters. At AQU, the fast directions obtained for the subvertical incidence angles (0°–15°) are oriented NW–SE, and the delay times are quite small (in the order of 0.060 s), while for *S* waves with 15°–45° incidence angle we found fast directions also oriented ∼NE–SW. For AQU, the average direction is well evident except for the presence of sparse orthogonal measures distributed over all the polar plot: these NE–SW measures seems to have a delay time higher than the other measures. Moreover at AQU, the polarization direction of larger δt seems to gently rotate moving from SE toward NE in the polar plot, suggesting that rays pass through a subvertical set of fractures, as predicted by the horizontal transverse isotropy (Backus 1962; Thomsen 1986). RM07 shows larger delay times with directions striking NNW, while smaller measures are clustered in the sector 150°N–250°N showing polarization direction striking NE. At RM26/LG03, the measures coming from the NW backazimuth sector are more homogeneous than those located in the other sectors.

Analysing the 'non-null' measures the station CAMP shows a sudden variation in polarization azimuth and in delay time magnitude for backazimuth between 170°N and 220°N. In this narrow backazimuth range, polarization directions pattern change from

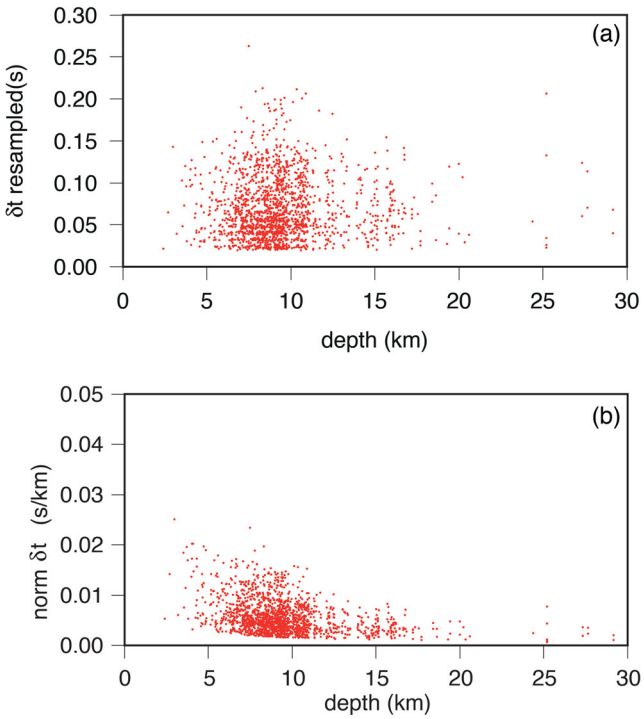

Figure 6. Plot showing (a) unnormalized resampled and (b) path-normalized delay time plotted versus the hypocentres depth for the whole data set of good splitting measurements.

about 160°N (SSE) to 110°N (ESE), while the overall delay times increase in the range 0.02–0.06 s.

3.2 Time delays of split shear waves and the depth extent of anisotropy

Individual measurements of delay time vary between 0.024 and 0.26 s. Time delay up to 0.3 s is quite common in the highly heterogeneous crust if the strength of anisotropy is high (Barruol & Mainprice 1993). The average value for the whole data set is $\delta t = 0.068 \pm 0.037$ s (Table S1). Similar δt values are in agreement with delay times found in other regions of Central Apennines in Italy (Margheriti *et al*. 2006; Piccinini *et al*. 2006; Pastori *et al*. 2009) or worldwide, (Saiga *et al*. 2003; Paulssen 2004; Peng & Ben-Zion 2004; Hiramatsu *et al*. 2005, 2010; Balfour *et al*. 2012). Fig. 6(a) shows the variation of the delay time with depth. Overall, we do not identify a clear increase of delay time with increasing events depth, suggesting a possible source of anisotropy in the uppermost crust. This trend is compatible with those observed in southern Hawaii (Munson *et al*. 1995), along the rupture zone of the 1999 Hector Mine earthquake (Cochran *et al*. 2003) and in Wellington region, New Zealand (Gledhill 1991). Along the 1999 Izmit Rupture, Northwest Turkey (Hurd & Bohnhoff 2012), the absence of correlation between the delay time and the depth lead the authors to confine the anisotropy upon the shallowest earthquakes, as also proposed in the Loma Pietra segment of the San Andreas Fault system (Zhang & Schwartz 1994) and in other regions (Savage *et al*. 1989).

In Figs S3(a) and (b) (Supplementary material), we plot the δt versus the hypocentral depth at stations with more than eight measurements; the stations are ordered from NW to SE. At most of these stations we observe that the delay time does not increase with depth. Higher value of δt, up to 0.2 s, are found at stations RM21, RM26/LG03, RM06 and RM07 and is associated to earthquakes located around 7 km depth.

To investigate the pattern of the delay time we also consider the normalized delay time [δt_{NORM}], calculated by dividing each time delay by ray length as commonly done in other studies (Liu *et al*. 1997; Gao *et al*. 2011; Martin *et al*. 2014). The advantage of this type of representation is to make comparable δt from events located at different depths (Gao *et al*. 1998; Crampin & Peacock 2005; Bianco *et al*. 2006). The average of the normalized δt for the single stations (Table S1) varies between 0.0014 and 0.0077 s km^{-1}, while the average value for the whole data set is 0.0056 s km^{-1}. In Fig. 6(b), we plot the path-normalized delay time versus hypocentral depth at all stations. Our results show δt_{NORM} larger than 0.02 s km^{-1} in the shallower layers, confirming the hypothesis that the upper crust could be the major source of anisotropy. The higher value of δt in the upper crust suggests a high concentration of EDA cracks and higher percentage of shear wave velocity anisotropy.

4 DISCUSSION

Our analysis points to a clear anisotropic behaviour of the crust that demonstrates the complex long-lasting history of tectonic deformation of the region and the 3-D variation of local stress orientation. The increased number and close spacing of seismic stations installed in the Abruzzi region and the large number of earthquakes recorded during the seismic sequence allowed us to map the distribution of fast shear wave measurements over the M_{w} 6.1 main shock source area and the surrounding region. The observed individual *S*-wave splitting data display strong spatial variability and complex pattern of crustal anisotropy. The lateral variation of fast direction is reasonably due to both stress and structural mechanisms, as suggested by the clear similarity between the local fault strike and the $\mathrm{SH_{max}}$. The rose diagram for the whole data set shows a predominant NNW–SSE orientation (N141°) of fast directions, almost perpendicular to the regional $\mathrm{Sh_{min}}$, as indicated by Carafa & Barba (2013) and also deduced from the World Stress Map (http://dc-app3-14.gfz-potsdam.de/pub/introduction/introduction_frame.html; Heidbach *et al*. 2008), and from the other stress indicators that indicate $\mathrm{SH_{max}}$ striking NW–SE (Fig. 4). Focal mechanism solutions computed by D'Amico *et al*. (2013) and Liu *et al*. (2009) using the earthquakes of the 2009 seismic sequence all feature a dominant normal faulting style with fault planes striking NW–SE. Similarly, Pondrelli *et al*. (2010), computing 26 CMT (Centroid Moment tensor) data, show *T*-axes perpendicular to the trend of the Apennines, revealing mechanisms with predominant normal faulting with ENE-extensional direction. Moreover, we should note that the orientation of the mean fast direction is also almost parallel to the averaged strike of the local normal faults.

The NNW–SSE orientation of fast directions is compared both with the fault strikes compilation available for the Central Apennines (Pizzi & Galadini 2009) and with the tectonic surface ruptures related to the 2009 earthquake (EMERGEO Working Group 2010; Fig. 4b). The frequency distribution of the Quaternary fault strikes clearly shows a preferred orientation of NW–SE, in agreement with the mean fast axis orientation. Moreover, ESE-striking faults are also represented, which could be related to the faults in the Gran Sasso Thrust as well as Campo Imperatore fault system. The rose diagram for the data set of tectonic surface ruptures again shows a well-defined orientation of NW–SE.

Delay times, both unnormalized and normalized, do not show any clear evidence of increasing with increasing depth. Similar

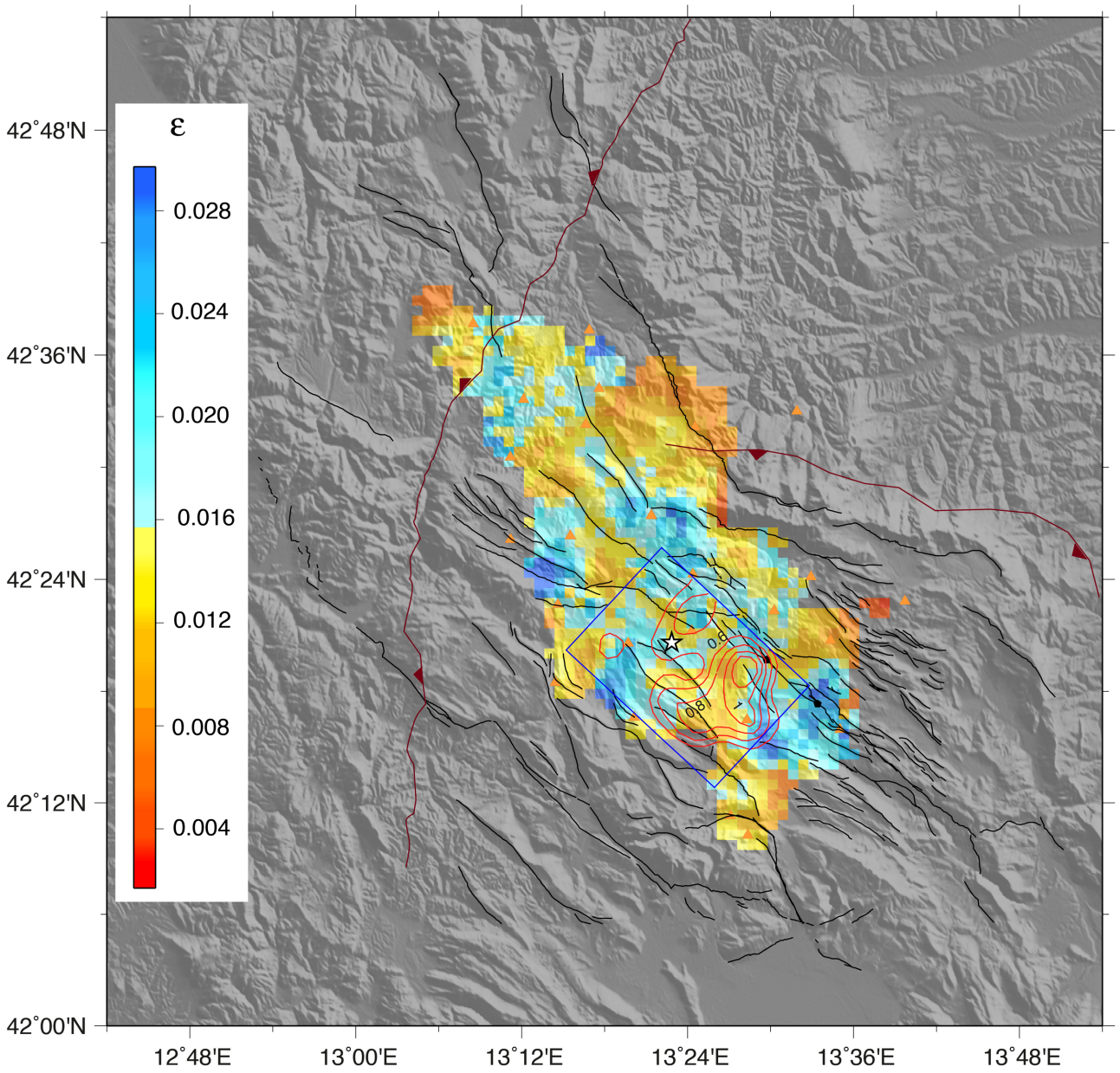

Figure 7. Representation of the crack density values (ε) interpolated on a regular grid. Individual values of ε were interpolated using a nearest neighbour algorithm (see the text for details). Blue box is the surface projection of the main shock fault plane as in Fig. 1. The red solid contours are the coseismic slip computed by Cirella *et al*. (2012). Black and dark red lines are the traces of the Quaternary active normal faults and of the main thrusts, respectively, as described in Fig. 1. The white star is the epicentre of the main shock; the orange triangles are the stations that return good splitting measurements.

results indicate that the anisotropy is confined primarily in shallower crustal structures, in accordance with other results suggesting that the anisotropy is kept in the upper crust (Cassidy & Bostock 1996; Currie *et al*. 2004).

Looking at the overall distribution of the splitting parameters in map view (Fig. S1 in the Supplementary material), we see that it is quite difficult to discern some spatial pattern for the fast axes. To better investigate the anisotropic pattern we therefore produce two maps showing the interpolated values of both crack density (Fig. 7) and the splitting parameters (Fig. 8). The delay time is a measure of the intensity of the anisotropy, which in turns is related to the crack density (ε) (Crampin 1994). We thus evaluate the average ε using the formula $\varepsilon = \beta(\delta t/L)$, where β is the average S-wave velocity, δt is the delay time and L is the propagation length (O'Connell & Budiansky 1974; Hudson 1981). Since most of our hypocentres are distributed between 6 and 14 km depth, we can therefore assume an average depth of ∼10 km. Considering $L = 10$ km, $\beta = 3.0$ km s^{-1} for carbonate rocks and the average $\delta t = 0.068$ s for the whole data set, we obtain an average value of $\varepsilon = 0.02$. Following Crampin (1994), this value is about to half of the 0.045 lower limit, above which the rocks became heavily fractured. To map the spatial distribution of the crack density (Fig. 7), the value of. ε was evaluated for each single delay time projected at the midpoint between source and receiver and then interpolated using a nearest neighbour algorithm. We used a nearest neighbour algorithm to interpolate our sparse δt measurements over a regular grid with 1 km spacing between nodes. The weighted average value of delay times falling within a 3 km radius was assigned to each node, if

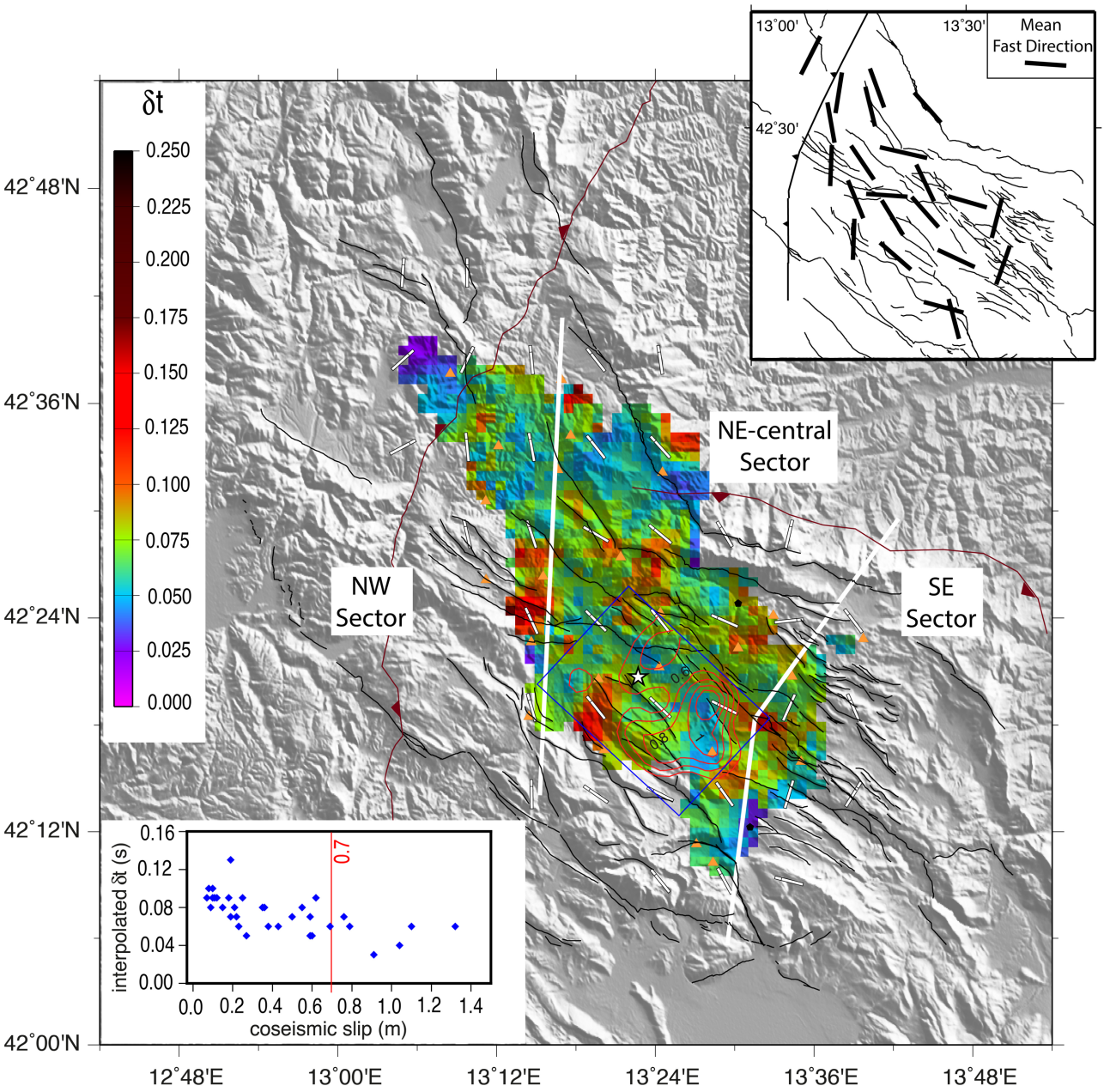

Figure 8. Representation of the anisotropic parameters on a regular grid**.** Individual values of δt were interpolated using a nearest neighbour algorithm, following the approach used for the interpolated crack density (see the text for details). We have also evaluated the average fast directions (white solid line) obtained smoothing the raw splitting measurements over a regular grid. For details on the red solid contours, the blue box and the black and dark red lines see Fig. 7. White star: epicentre of the main shock; orange triangles: stations that return good splitting measurements. We recognize three different sector, each one characterized by a peculiar trend of φ: the NE-central sector, with predominant NNW–SSE oriented φ; the NW sector, with φ almost N–S oriented and the SE sector, with most of φ oriented NE–SW. In the upper right inset are reported the distribution of the mean fast directions for stations with $\geq$8 good measurements. The diagram in the upper right corner shows the comparison between δt and slip within the ruptured area (see the text for details). High values of coseismic slip (>0.7 m) are associated to low values of delay times (∼0.06 s).

there is at least one value inside each of the 24 15° azimuthal sectors. The same averaging procedure over a regular grid was applied on the splitting parameters δt and using the appropriate directional average functions on the φ. The results are shown in Fig. 8: the smoothed value of delay times are given by the colour scale, while the interpolated φ are shown as white solid bars. We applied this simple averaging method because we did not observe a strong azimuthal dependence of the splitting parameter, implying our results did not require the application of a delay time tomography technique (Johnson *et al*. 2011). To better understand the relationships of the spatial distribution of the crack density and splitting parameters versus the crustal deformation induced by the 2009 L'Aquila earthquakes, on both the figures we superimposed the surface projection of the main shock fault plane along with the patches of the larger coseismic slip (Cirella *et al*. 2012). In general, we observe that the study area is characterized by variable crack density and delay time, implying the presence of a well-developed anisotropic fractured rock mass.

We note that there is a clear inverse correlation between the regions of the fault with large slip and higher crack density and delay time. In the area of main fault (black rectangle in Fig. 7), we note that higher value of ε (>0.016) and of δt (>0.1 s) are confined at the edges of the main fault patches that ruptured with the M_w 6.1 main shock, while the lower values of ε (<0.016) and of δt (<0.1 s) are confined in the central part of the fault, where the coseismic slip is higher. This is also well represented in the inset in Fig. 8, in which the slip has been compared quantitatively to the delay time within the fault area. The measures of two physical quantities have uneven spatial distribution in the volume encompassing the main shock fault plane. To make a comparison between delay time and slip we therefore resampled δt and slip by a new interpolation over the fault plane surface projection using a regular 2-km grid (we choose this value because the slip points are more widely spaced than the delay times). Then, for each point we plotted the corresponding interpolated δt and slip values. It is quite clear that high values of coseismic slip (>0.7 m) are associated to low values of delay times ($\sim$0.06 s). At the borders of the main shock fault plane, where coseismic slip tapers to zero, there is much scatter in delay times and values up to 0.13 s are found.

We can assume that the edges of the fault could act as a rheological barrier caused by lateral variations in crustal structure (as also suggested by Di Stefano *et al*. 2011 and Cirella *et al*. 2012). In this case, the presence of the barrier could be responsible for overpressurized fluids conditions, while within the main shock rupture area high-energy release resulted in an open crack system, such that high-pressure condition are not possible.

In the following, we subdivided the study region into three different sectors (central and northeastern sector; northwestern sector; southeastern sector), each one characterized by a different anisotropic pattern. This leads us to hypothesis that multiple competing and interacting mechanisms contribute with different intensity to the observed anisotropy.

4.1 Central and northeastern sector

In the central and northeastern parts of the study area, the averaged direction of fast axes shows an orientation generally coherent and changing accordingly with the strike of the major Quaternary normal faults (Galadini & Galli 2000; Ghisetti & Vezzani 2002; Pizzi *et al*. 2002; Boncio *et al*. 2010; Schlagenhauf *et al*. 2010; Pucci *et al*. 2014). The match between the fast polarization directions and the strike of the faults could be related to the complex network of micro- and mesoscale structures (small faults, shear fractures, joints, pressure-solution surfaces) aligned preferentially parallel to the main fault, which develop in the damage zone as the blocks on both sides of the fault move relative to each other (Ben-Zion & Sammis 2003). Such an alignment gives rise to a distribution of fault-parallel φ as predicted by the structure-related anisotropy model (Zinke & Zoback 2000). This result is consistent with other findings in China (Liu *et al*. 2004, 2005; Gao *et al*. 1995, 2011; Shi *et al*. 2006; Wu *et al*. 2009), California (Savage *et al*. 1990; Cochran *et al*. 2006) and Brazil (do Nascimento *et al*. 2002). Moving towards the northeastern sector of the study area, we observe that the strike of faults slightly deviates from the general NW–SE direction and the fast axes rotate accordingly. In fact, the station RM26/LG03 and RM08 have fast axes oriented WNW–ESE, as the Assergi fault, while moving towards RM32, RM11 and CAMP stations fast axes rotate to N–S to follow the NNW traces of the Montereale and the Laga faults (Galadini & Galli 2000). Similar rotation is also observed at the station PRE1, located on the Pettino-Arischia active fault, oriented WNW–ESE (Blumetti & Guerrieri 2007) and return an E–W mean fast direction.

In the southweastern sector, the rotation of the fast axes from NW–SE to E–W to mark the strike of the local faults is particularly evident when moving from the station RM24, located on the Piano di Pezza fault (Villani *et al*. 2015a,b) to the station RM04, located on the northwest tip of the Ovindoli-Celano fault-systems (Pantosti *et al*. 1996; Salvi *et al*. 2003).

The NW–SE fast polarization directions in the central part are also in accordance with the direction of the SH_{max}. This is common in the extensional regimes, as in the Abruzzi region, where SH_{max} coincides with the strike of the main faults. A similar pattern of fast directions is generally attributed to a widespread distribution of vertically, fluid-saturated EDA cracks: the faster polarized shear waves are parallel to the strike of the EDA microcracks and, together, are polarized in the direction of the maximum horizontal compressive stress (Gao *et al*. 1995, 2009; Leitner *et al*. 2001; Balfour *et al*. 2005; Sibson *et al*. 2011). It is, therefore, possible that the shear wave splitting observed in our study region within the fault zone and the surrounding crust could also be driven by the presence of local fluid-filled crack system oriented almost in the direction of the main structural lineaments. The presence of fluid-saturated crack has also been supported by high value of *Vp/Vs* (up to 1.95) found in the region, supporting the hypothesis that fluid-rich zones are present within the seismogenic volume of the L'Aquila sequence (Di Luccio *et al*. 2010). However, the consistency between the orientation of fast axes with both the local fault trace and the regional trend of SH_{max} making it quite difficult to isolate the stress-induced contribution from the structural one suggesting the hypothesis that both mechanisms act at the same time (Peng & Ben-Zion 2004; Liu *et al*. 2008; Hurd & Bohnhoff 2012; Eken *et al*. 2013).

4.2 Northwestern sector

In the northwestern edge of the area, we observe a reorganization of the fast directions from NNE–SSW (station RM21) to N–S (stations RM29, RM11 and RM09). These stations are located close to the OAL, which is a regional overthrust consisting of a complex set of crustal thrust ramps and oblique-slip faults, generally trending NE, and >100 km long. Pizzi & Galdini (2009) suggest that this first-order crustal structure represents a barrier separating two different active and seismogenic extensional fault systems (the Norcia and Mt. Vettore faults to the northeast and the Laga Fault to the southwest). Moreover, they also note that this region displays moderate background historical and instrumental seismicity that could represent the activation of some minor transfer structures between the main aforementioned normal fault systems. These small transfer structures are commonly observed in the overstep areas of main extensional faults (Leeder & Gawthorpe 1987) and were also reported by Bagh *et al*. (2007) in a study of microseismicity in the central-southern Abruzzi. It is possible that the OAL and the minor associated transfer structures control the rotation of fast directions from NNE–SSW to N–S.

4.3 Southeastern sector

The anisotropic pattern becomes more complicated in the southeastern sector of the region, where fast directions significantly diverge from the regional $SH_{max,}$ direction as well as from the trend of the major normal faults. In particular, at the FAGN and RM14

stations we found that the mean fast direction is oriented almost perpendicular to SH_{max} and to the strike of the faults. In addition, the southeastern sector returns the highest value of delay time. Fig. 8 clearly shows pockets of large value of delay times, >0.07 s, combined with interpolated fast direction oriented normal to the SH_{max}. The 90° flip associated with increase in delay time suggests that the rock volume here underwent different physical condition with respect to the surrounding rock, which is probably related to pore-pressure changes, stress and fracture field variations as well as fluid migrations. In order to exclude any effect related to the cycle skipping problem, we carefully inspected the corrected and shifted waveforms to ensure that the 90° flipped direction was not due to a technical problem. There could be at least two main mechanisms that can explain this behaviour. The first mechanism is the presence of heavily fractured and overpressurized rock volumes. In this case, microcracks are filled at high pressure and the fast and slow component rotate by 90°. Indeed, increasing pore-fluid pressure reorganizes the geometry of the microcracks, which will be no longer uniformly oriented by the regional active stress field along the direction of the maximum compressive stress. In this case, the fast and slow components rotate by 90°, becoming orthogonal to the plane of the cracks (90° flips) (Zatsepin & Crampin 1997; Angerer *et al*. 2002; Crampin *et al*. 2002, 2004; Padhy & Crampin 2006). This is in agreement with the higher crack density and delay time observed in the southeastern sector. Increment in pore-fluid pressure is also suggested by the progressive increase of *Vp/Vs* (up to 1.95) during the seismic sequence, indicating the presence of overpressurized fluid traps within the crust (Di Luccio *et al*. 2010). Moreover, in the southeastern sector large (up to 10 times) amplitude fault-zone trapped waves were observed, as reported by Calderoni *et al*. (2012) at station FAGN. Trapped waves require a low-velocity fault zone originated by different factors such as dilatant cracks, fluids concentrated near faults, and increased porosity (Sibson 1977; Wang 1984; Li & Leary 1990). Events responsible for the trapped waves recorded at FAGN are clustered at the southeastern bottom end of the fault responsible of the main shock fault. This cluster is located within a seismogenic volume characterized by highest excess of fluid pressure as inferred by the focal mechanism tomography (Terakawa *et al*. 2013). In this case, the particle motion could be rearranged following the anomalous amplification of the horizontal component of the seismograms.

The second mechanism is the presence of faults that are aligned at high angle with the dominant strike of the major Quaternary faults in the area. In fact, the fast polarization directions can diverge up to 90° from the direction of crack strike in case of intersecting fracture systems (Rial *et al*. 2005). In this case, the resulting geometry of cracks is more complicated than the simple vertical distribution. Fast directions recorded at FAGN are located where a sharp cut-off (Fig. 1, inset) of the 2009 aftershocks sequence is located (Chiaraluce *et al*. 2011; Valoroso *et al*. 2013). This could be related to a deep set of NNE-trending faults that act as a boundary between the major seismogenic structures of the Paganica-San Demetrio fault systems to the northwest and the Middle Aterno Valley faults to the southeast. Recently published geological maps (Pucci *et al*. 2014) and integrated shallow geophysical investigations (microtremor analyses, electrical resistivity tomography and time-domain electromagnetic soundings) between L'Aquila and San Demetrio towns suggest that NNE-trending normal faults played a major role in the Early Pleistocene, prior to the activation of the Paganica-San Demetrio fault systems (Civico *et al*. 2015b). It is possible that these faults, although shorter and more fragmented than the NW-trending faults, may control the distribution of microseismicity. Moreover, at the southeastern part of the study area, the sharp termination of the Middle Aterno basin could suggest the presence of a deep buried NNE-SSW structure. This inherited structure does not produce evident recent deformation at the surface but could control the lateral extension of the crustal faults affecting the central portion of the study area. This deep structural element could represent an obstruction to the fluid flows from the main shock area, promoting overpressure phenomena in weak and fluid saturated faults. This is reflected in the *S*-wave anisotropy pattern caused by the dominant fracture orientation. Recall the 90° flip of fast axes with the associated pockets of high δt; the abrupt cut-off of seismicity, with hypocentres distributed along an NE–SW oriented plane; the abrupt termination to southeast of the Middle Aterno fault systems and the presence of the deep buried NE–SW structure we can explain the anisotropic pattern in the southeastern sectors as due to the presence of a transition zone that act as a barrier for the fluids that escape from the hypocentral area during the nucleation. It is therefore possible that events recorded at FAGN and RM14 passed through heavily fractured and overpressurized rock volumes while the other stations, in which the ray paths come from a different area and sample a different volume of rock, record the effects of the fracture field generated by the regional stress field.

5 CONCLUSIONS

In this work, we present a detailed map of seismic anisotropy in the Abruzzi region obtained using thousands of earthquakes recorded during the 2009 April 6 L'Aquila seismic sequence by 55 closely spaced stations operating in the area. The results have shown the existence of a well defined but complex anisotropic structure beneath the region. We relate the observed pattern as due to the combination of both the shear fabric of the fault zones, and to the presence of a widespread distribution of stress-aligned fluid-saturated cracks. In Fig. 9, we represent a sketch summarizing the different mechanisms generating shear wave splitting in the crust in the different sectors of the study area, according to our interpretation. SAM is observed at the station located in the central, northwestern and northeastern sectors, where fast polarization direction are predominantly aligned NW–SE and thus parallel to the strike of local faults. At some stations, fast axes deviate from NW–SE and change their orientations accordingly to the strike of the faults. However, fast directions in the central sector are also aligned parallel to the maximum horizontal stress active in the region, suggesting the role of stress-induced anisotropy (EDA) driven by the presence of local fluid-filled crack system oriented almost in the direction of the main structural lineaments. At the southeastern part of the region fast directions change their orientation to become orthogonal to the strike of fault and to the SH_{max}. Such deviations from the general trend are explained by local structural complexities related to deep buried NE–SW fault systems, or by zones bearing overpressurized fluids which are responsible for the 90° flips of fast axes and the generation of trapped waves.

Delay times do not show any variations with depth, supporting the hypothesis that most of the anisotropy is confined in the uppermost crust. Notably, on an averaged map lower delay times correspond to the regions of the main shock fault plane (black box in Fig. 8) where large slip occurred, whereas lower values are confined to the edges of the rupture patches.

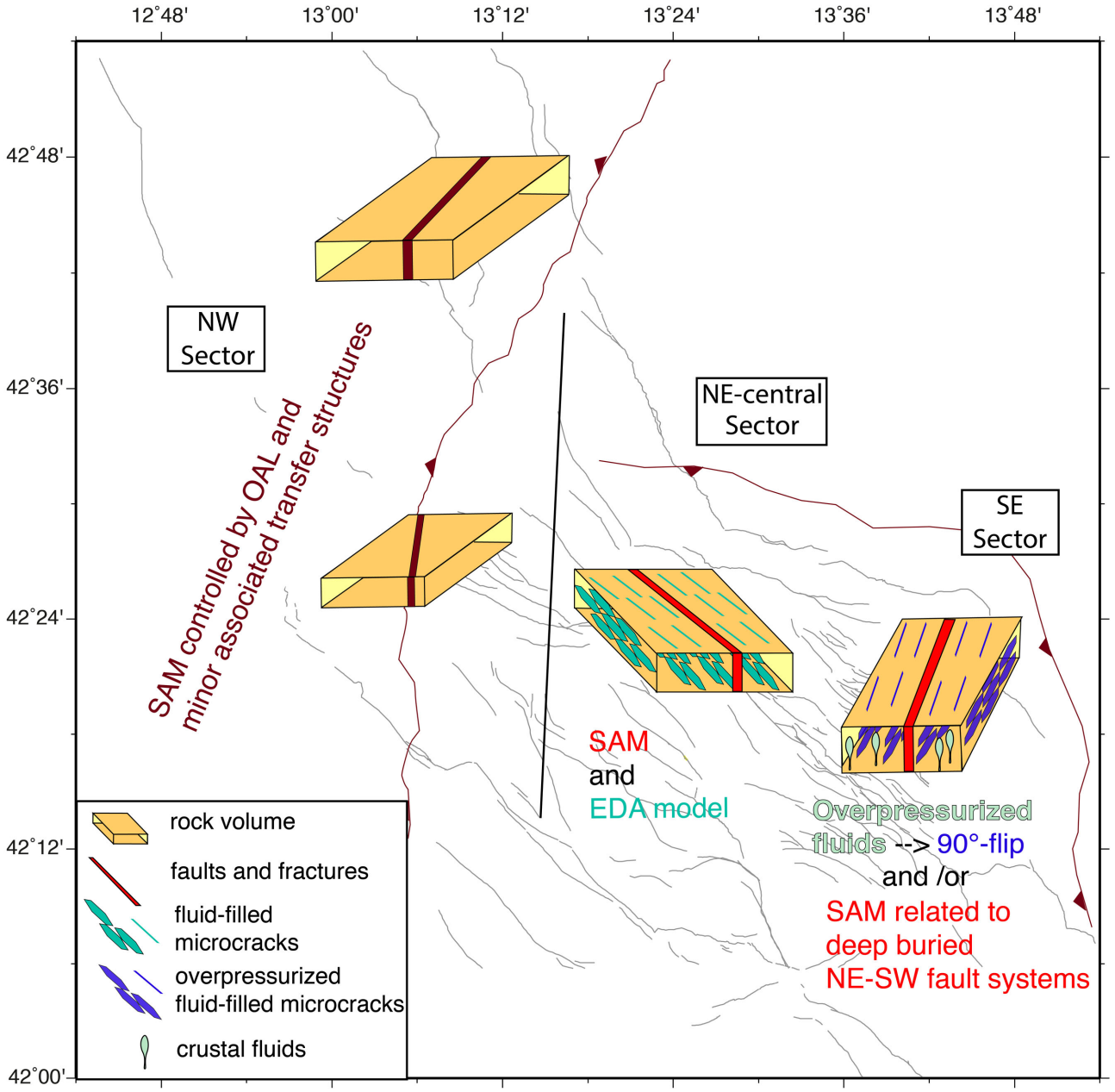

Figure 9. Sketch summarizing the two models of anisotropy in the Abruzzi region: structural-controlled anisotropy model (here called SAM) and stress-induced anisotropy model (EDA). In the northwestern sector, the anisotropy is controlled by the Olevano-Antrodoco Line and associated minor transfer structures, which cause fast axes oriented NNE–SSW and N–S (see the black bars in the upper right inset of Fig. 8). In the central sector, the anisotropy is presumably controlled by the combination of both faults and fracture alignments, as predicted by SAM and by the fluid-filled microcracks alignments, as predicted by EDA. To the southeast, the fast directions are oriented normal to the regional SH_{max}, direction and to the strike of the major normal faults. This pattern is thought to be caused by two main mechanisms: (1) the presence of heavily fractured and overpressurized rock volumes: in such a case, the increasing pore-fluid pressure causes the 90° flips of the fast axes; (2) the presence of buried NE–SW fault systems, which primarily control the orientations of fast directions.

ACKNOWLEDGEMENTS

We are grateful to Lauro Chiaraluce, Raffaele Di Stefano and Luisa Valoroso for making available the catalogue of earthquakes location and phase picking file. We thank Vanja Kastelic for providing us the georeferenced faults after Schlagenhauf *et al*. (2010) and Antonella Cirella for supplying coseismic slip values. We acknowledge Fabio Villani for the constructive discussions and suggestions about the geological setting of the Abruzzi region. We thank Gaetano De Luca for providing us the data recorded at the INGV permanent regional seismic network of the Abruzzi region. We also acknowledge the Editor Gabi Laske and the reviewers Robert Porrit and Martha Savage for their valuable criticisms and comments, which helped to improve the quality of the manuscript. We thank Shane Murphy for useful suggestions. Paola Baccheschi is supported by MIUR-FIRB Abruzzo project 'High-resolution analyses for assessing the seismic hazard and risk of the areas affected by the 2009 April 6 earthquake' (funding code: RBAP10ZC8K_003). All figures were made using the GMT software (Wessel & Smith 1998).

REFERENCES

Aldersons, F., Di Stefano, R., Chiaraluce, L., Piccinini, D. & Valoroso, L., 2009. Automatic detection, and *P* and *S* wave picking algorithm: an application to the 2009 L'Aquila (central Italy) earthquake sequence, *EOS, Trans. Am. geophys. Un.*, **90**(52), Fall Meet. Suppl., Abstract U23B-0045, Poster.

Angerer, E., Crampin, S., Li, X.-Y. & Davis, T., 2002. Processing, modelling, and predicting time-lapse effects of over-pressured fluid injection in a fractured reservoir, *Geophys. J. Int.*, **149**, 267–280.

Aster, R.C. & Shearer, P., 1992. Initial shear wave particle motions and stress constraints at the Anza seismic network, *Geophys. J. Int.*, **108**, 740–748.

Backus, G.E., 1962. Long-wave elastic anisotropy produced by horizontal layering, *J. geophys. Res.*, **67**, 4427–4440.

Bagh, S., Chiaraluce, L., De Gori, P., Moretti, M., Govoni, A., Chiarabba, C., Di Bartolomeo, P. & Romanelli, M., 2007. Background seismicity in the central Apennines of Italy: the Abruzzo region case study, *Tectonophysics*, **444**, 80–92.

Bagnaia, R., D'Epifanio, A. & Sylos Labini, S., 1992. Aquila and subaequan basins: an example of Quaternary evolution in central Apennines, Italy, *Quat. Nova*, **II**, 187–209.

Balfour, N.J., Cassidy, J.F. & Dosso, S.E., 2012. Crustal anisotropy in the forearc of the Northern Cascadia Subduction Zone, British Columbia, *Geophys. J. Int.*, **188**, 165–176.

Balfour, N.J., Savage, M. & Townend, J., 2005. Stress and crustal anisotropy in Marlborough, NewZealand: evidence for low fault strength and structure controlled anisotropy, *Geophys. J. Int.*, **163**(3), 1073–1086.

Barchi, M. *et al.*, 2000. Sintesi delle conoscenze sulle faglie attive in Italia centrale, *Report Gruppo Naz. per la Difesa dai Terremoti*, Rome.

Barruol, G. & Mainprice, D., 1993. A quantitative evaluation of the contribution of crustal rocks to shear-wave splitting of teleseismic SKS waves, *Phys. Earth planet. Inter.*, **78**, 281–300.

Ben-Zion, Y. & Sammis, C.G., 2003. Characterization of fault zones, *Pure appl. Geophys.*, **160**, 677–715.

Bianco, F., Scarfì, L., Del Pezzo, E. & Patanè, D., 2006. Shear wave splitting changes associated with the 2001 volcanic eruption on Mt Etna, *Geophys. J. Int.*, **167**, 959–967.

Bigi, S. & Pisani, P.C., 2005. From a deformed peri-Tethyan carbonate platform to a fold and thrust-belt: an example from the central Apennines (Italy), *J. Struct. Geol.*, **27**, 523–539.

Blumetti, A.M., Di Filippo, M., Zaffiro, P., Marsan, P. & Toro, B., 2002. Seismic hazard of the city of L'Aquila (Abruzzo-central Italy): new data from geological, morphotectonic and gravity prospecting analysis, *Studi Geol. Camerti.*, **1**, 7–18.

Blumetti, A.M. & Guerrieri, L., 2007. Fault-generated mountain fronts and the identification of fault segments: implications for seismic hazard assessment, *Boll. Soc. Geol. It.*, **126**(2), 307–322.

Boncio, P., Lavecchia, G. & Pace, B., 2004. Defining a model of 3D seismogenic sources for seismic hazard assessment applications: the case of central Apennines (Italy), *J. Seismol.*, **8**, 407–425.

Boncio, P., Pizzi, A., Brozzetti, F., Pomposo, G., Lavecchia, G., Di Naccio, D. & Ferrarini, F., 2010. Coseismic ground deformation of the 6 April 2009 L'Aquila earthquake (central Italy, M_w 6.3), *Geopys. Res. Lett.*, **37**, L06308, doi:10.1029/2010GL042807.

Boness, N.L. & Zoback, M.D., 2004. Stress-induced seismic velocity anisotropy and physical properties in the SAFOD pilot hole in Parkfield, CA, *Geophys. Res. Lett.*, **31**, L15S17, doi:10.1029/2003GL019020.

Boness, N.L. & Zoback, M.D., 2006. Mapping stress and structurally controlled crustal shear velocity anisotropy in California, *Geology*, **34**, 825–828.

Booth, D.C. & Crampin, S., 1895. Shear-wave polarizations on a curved wavefront at anisotropic free surface, *Geophys. J. R. astr. Soc.*, **83**, 31–45.

Bouin, M.P., Téllez, J. & Bernard, P., 1996. Seismic anisotropy around the Gulf of Corinth, Grrece, deduced from the three-component seismograms of local earthquakes and its relationship with crustal strain, *J. geophys. Res.*, **101**, 5797–5811.

Bowman, J.R. & Ando, M., 1987. Shear-wave splitting in the upper-mantle wedge above the Tonga subduction zone, *Geophys. J. R. astr. Soc.*, **88**, 25–41.

Brocher, T.M. & Christensen, N.I., 1990. Seismic anisotropy due to preferred mineral orientation observed in shallow crustal rocks in southern Alaska, *Geology*, **18**, 737–740.

Buontempo, L. & Wuestefeld, A., 2013. Complex fault structure interactions of crustal shear zones revealed by seismic anisotropy: an example in the eastern betic cordillera (Spain), *TerraNova*, **25**, 57–64.

Calamita, F. & Deiana, G., 1988. The arcuate shape of the Umbria–Marche–Sabina Apennines (central Italy), *Tectonophysics*, **146**, 139–147.

Calderoni, G., Di Giovambattista, R., Vannoli, P., Pucillo, S. & Rovelli, A., 2012. Fault-trapped waves depict continuity of the fault system responsible for the 6 April 2009. 6.3 L'Aquila earthquake, central Italy, *Earth planet. Sci. Lett.*, **323–324**, 1–8.

Carafa, M. & Barba, S., 2013. The stress field in Europe: optimal orientations with confidence limits, *Geophys. J. Int.*, **193**, 531–548.

Cassidy, J.F. & Bostock, M.G., 1996. Shear-wave splitting above the subducting Juan de Fuca Plate, *Geophys. Res. Lett.*, **23**, 941–944.

Castellarin, A., Colacicchi, R., Praturlon, A. & Cantelli, C., 1982. The Jurassic-Lower Pliocene history of Ancona-Anzio line (central Italy), *Mem. Soc. Geol. Ital.*, **24**, 325–336.

Cavinato, G.P. & De Cellis, P.G., 1999. Extensional basins in the tectonically bimodal central Apennines fold-thrust belt, Italy: response to corner flow above a subduction slab in retrograde motion, *Geology*, **27**, 955–958.

Cheloni, D. *et al.*, 2014. Coseismic and post-seismic slip of the 2009 L'Aquila (central Italy) M_w 6.3 earthquake and implications for seismic potential along the Campotosto fault from joint inversion of high-precision levelling, InSAR and GPS data, *Tectonophysics*, **622**, 168–185.

Chiarabba, C. *et al.*, 2009. The 2009 L'Aquila (central Italy) M_w 6.3 earthquake: main shock and aftershocks, *Geophys. Res. Lett.*, **36**, L18308, doi:10.1029/2009GL039627.

Chiaraluce, L., Valoroso, L., Piccinini, D., Di Stefano, R. & De Gori, P., 2011. The anatomy of the 2009 L'Aquila normal fault system (central Italy) imaged by high resolution foreshock and aftershock locations, *J. geophys. Res.*, **116**, B12311, doi:10.1029/2011JB008352.

Cirella, C., Piatanesi, A., Tinti, E., Chini, M. & Cocco, M., 2012. Complexity of the rupture process during the 2009 L'Aquila, Italy, earthquake, *Geophys. J. Int.*, **190**, 607–621.

Civico, R., Pucci, S., De Martini, P.M. & Pantosti, D., 2015a. Morphotectonic analysis of the long-term surface expression of the 2009 L'Aquila earthquake fault (Central Italy) using airbone LiDAR data, *Tectonophysics*, **644–645**, 108–121.

Civico, R. *et al.*, 2015b. Imaging the three-dimensional architecture of the Middle-Aterno basin (2009 L'Aquila earthquake, Central Italy) using ground TDEM and seismic noise surveys: preliminary results, in *Abstract Volume 6th International INQUA Meeting on Paleoseismology, Active Tectonics and Archaeoseismology, 19–24 April 2015, Pescina, Fucino Basin, Italy*, Vol. 27, pp. 83–87, eds Blumetti, A.M., Cinti, F.R., De Martini, P.M., Galadini, F., Guerrieri, L., Michetti, A.M., Pantrosti, D. & Vittori, E., Miscellanea, INGV.

Cochran, E.S., Li, Y.-G. & Vidale, J.E., 2006. Anisotropy in the shallow crust observed around the San Andreas fault before and after the 2004 M 6.0 Parkfield earthquake, *Bull. seism. Soc. Am.*, **96**, S364–S375.

Cochran, E.S., Vidale, J.E. & Li, Y.-G., 2003. Near-fault anisotropy following the Hector Mine earthquake, *J. geophys. Res.*, **108**(9), 2436, doi:10.1029/2002JB002352.

Crampin, S., 1978. Seismic-wave propagation through a cracked solid: polarization as a possible dilatancy diagnostic, *Geophys. J. R. astr. Soc.*, **53**, 467–496.

Crampin, S., 1994. The fracture criticality of crustal rocks, *Geophys. J. Int.*, **118**, 428–438.

Crampin, S. & Chastin, S., 2003. A review of shear wave splitting in the crack-critical crust, *Geophys. J. Int.*, **155**, 221–240.

Crampin, S. & Gao, Y., 2008. A review of the New Geophysics: a new understanding of pre-fracturing deformation in the crack-critical crust with implications for hydrocarbon production, *Petrol. Sci.*, **5**, 1–12.

Crampin, S. & Lovell, J.H., 1991. A decade of shear-wave splitting in the Earth's crust: what does it mean? what use can we make of it? and what should we do next?, *Geophys. J. Int.*, **1**(107), 387–407.

Crampin, S. & Peacock, S., 2005. A review of shear-wave splitting in the compliant crack-critical anisotropic Earth, *Wave Motion*, **41**, 59–77.

Crampin, S., Peacock, S., Gao, Y. & Chastin, S., 2004. The scatter of time delays in shear-wave splitting above small earthquakes, *Geophys. J. Int.*, **156**, 39–44.

Crampin, S., Volti, T., Chastin, S., Gudmundsson, A. & Stefánsson, R., 2002. Indication of high pore-fluid pressures in a seismically-active fault zone, *Geophys. J. Int.*, **151**, F1–F5.

Currie, C., Cassidy, J., Hyndman, R. & Bostock, M., 2004. Shear wave anisotropy beneath the Cascadia Subduction Zone and western North American craton, *Geophys. J. Int.*, **157**, 341–353.

D'Agostino, N., Avallone, A., Cheloni, D., D'Anastasio, E., Mantenuto, S. & Selvaggi, G., 2008. Active tectonics of the Adriatic region from GPS and earthquake slip vectors, *J. geophys. Res.*, **113**, B12413, doi:10.1029/2008JB005860.

D'Amico, S., Orecchio, B., Presti, D., Neri, G., Wu, W., Sandu, I., Zhu, L. & Herrmann, R.B., 2013. Source parameters of small and moderate earthquakes in the area of the 2009 L'Aquila earthquake sequence (central Italy), *Phys. Chem. Earth*, **63**, 77–91.

Davis, J.C., 1986. *Statistics and Data Analysis in Geology*, John Wiley, 646 pp.

Di Luccio, F., Ventura, G., Di Giovambattista, R., Piscini, A. & Cinti, F.R., 2010. Normal faults and thrusts reactivated by deep fluids: the 6 April 2009 M_w 6.3 L'Aquila earthquake, central Italy, *J. geophys. Res.*, **115**, B06315, doi:10.1029/2009JB007190.

Di Stefano, R., Aldersons, F., Kissling, E., Baccheschi, P., Chiarabba, C. & Giardini, D., 2006. Automatic seismic phase picking and consistent observation error assessment: application to the Italian seismicity, *Geophys. J. Int.*, **165**, 121–134.

Di Stefano R., Chiarabba, C., Chiaraluce, L., Cocco, M., De Gori, P., Piccinini, D. & Valoroso, L., 2011. Fault zone properties affecting the rupture evolution of the 2009 (M_w 6.1) L'Aquila earthquake (Central Italy): insights from seismic tomography, *Geophys. Res. Lett.*, **38**, L10310, doi:10.1029/2011GL047365.

do Nascimento, A., Pearce & Takeya, M., 2002. Local shear-wave observations in João Câmara, NE Brazil, *J. geophys. Res.*, **107**, 2232–2242.

Eken, T., Bohnhoff, M., Bulut, F., Can, B. & Aktar, M., 2013. Crustal anisotropy in the Eastern Sea of Marmara Region in Northwestern Turkey, *Bull. seism. Soc. Am.*, **103**(2A), 911–924.

EMERGEO Working Group, 2010. Evidence for surface rupture associated with the M_w 6.3 L'Aquila earthquake sequence of April 2009 (central Italy), *TerraNova*, **22**, 43–51.

Frietsch, M., Groos, J.C. & Ritter, J.R.R., 2015. Detection and delineation of a fracture zone with observation of seismic shear wave anisotropy in the Upper Rhine Graben, SW Germany, *Pure appl. Geophys.*, **172**, 267–282.

Galadini, F. & Galli, P., 2000. Active tectonics in the central Apennines (Italy)—input data for seismic hazard assessment, *Nat. Hazards*, **22**, 225–268.

Gao, Y. & Crampin, S., 2008. Shear-wave splitting and Earthquake forecasting, *TerraNova*, **20**(6), 440–448.

Gao, Y., Wang, P.-D., Zheng, S.-H., Wang, M., Chen, Y.-T. & Zhou, H.-L., 1998. Temporal changes in shear-wave splitting at an isolated swarm of small earthquakes in 1992 near Dongfang, Hainan Island, southern China, *Geophys. J. Int.*, **135**, 102–112.

Gao, Y., Wu, J., Cai, J.-A., Shi, Y.-T., Lin, S., Bao, T. & Li, Z.-N., 2009. Shear-wave splitting in southeast of Cathaysia block, South China, *J. Seismol.*, **13**, 267–275.

Gao, Y., Wu, J., Fukao, Y., Shi, Y. & Zhu, A., 2011. Shear wave splitting in the crust in North China: stress, faults and tectonic implications, *Geophys. J. Int.*, **187**, 642–654.

Gao, Y., Zheng, S.-H. & Sun, Y., 1995. Crack-induced anisotropy in the crust from shear wave splitting observed in Tangshan region, North China, *Acta Seismol. Sin.* (English Edition), **8**, 351–363.

Ghisetti, F. & Vezzani, L., 2002. Normal faulting, transcrustal permeability and seismogenesis in the Apennines (Italy), *Tectonophysics*, **348**, 155–168.

Gledhill, K.R., 1991. Evidence for shallow and pervasive seismic anisotropy in the Wellington region, New Zealand, *J. geophys. Res.* **96**(B13), 21 503–21 516.

Heidbach, O., Tingay, M., Barth, A., Reinecker, J., Kurfeß, D. & Muüller, B., 2008. The World Stress Map database release 2008, doi:10.1594/GFZ.WSM.Rel2008 (Last update, August 2009).

Herrmann, R.B., Malagnini, L. & Munafò, I., 2011. Regional moment tensors of the 2009 L'Aquila earthquake sequence, *Bull. seism. Soc. Am.*, **101**(3), 975–993.

Hiramatsu, Y., Honma, H., Saiga, A., Furumoto, M. & Ooida, T., 2005. Seismological evidence on characteristic time of crack healing in the shallow crust, *Geophys. Res. Lett.*, **32**, L09304, doi:10.1029/2005GL022657.

Hiramatsu, Y., Iwatsuki, K., Ueyama, S. & Iidaka, T. & Japanese University Group, 2010. Spatial variation in shear wave splitting of the upper crust in the zone of inland high strain rate, central Japan, *Earth Planets Space*, **62**, 675–684.

Hudson, J.A., 1981. Wave speeds and attenuation of elastic waves in material containing cracks, *Geophys. J. R. astr. Soc.*, **64**, 133–150.

Hurd, O. & Bohnhoff, M., 2012. Stress- and Structure-Induced shear-wave anisotropy along the 1999 Izmit Rupture, Northwest Turkey, *Bull. seism. Soc. Am.*, **102**(5), 2177–2188.

Johnson, J.H., Savage, M.K. & Townend, J., 2011. Distinguishing between stress-induced and structural anisotropy at Mount Ruapehu Volcano, New Zealand, *J. geophys. Res.*, **116**, B12303, doi:10.1029/2011JB008308.

Kaneshima, S., 1990. Origin of crustal anisotropy—shear-wave splitting studies in Japan, *J. geophys. Res.*, **95**(B7), 11 121–11 133.

Kendall, J.-M. *et al.*, 2007. Seismic anisotropy as an indicator of reservoir quality in siliciclastic rocks, *Geol. Soc. Lond., Spec. Publ.*, **292**, 123–136.

Kern, H. & Wenk, H.-R., 1990. Fabric-related velocity anisotropy and shear wave splitting in rocks from the Santa Rosa mylonite zone, California, *J. geophys. Res.* **95**, 11 213–11 223.

Leary, P., Crampin, S. & Mcevilly, T., 1990. Seismic fracture anisotropy in the Earth's crust-an overview, *J. geophys. Res.*, **95**, 11 105–11 114.

Leeder, M.R. & Gawthorpe, R.L., 1987. Sedimentary models for extensional tilt-block/half-graben basins, in *Continental Extensional Tectonics*, Geol. Soc. Lond. Spec. Publ., Vol. 28, pp. 139–152, eds Coward, M.P., Dewey, J.F. & Hancock, P.L., Geological Society London.

Leitner, B., Eberhart-Phillips, D., Anderson, H. & Nabelek, J., 2001. A focused look at the Alpine Fault, New Zealand: seismicity, focal mechanisms and stress observations, *J. geophys. Res.*, **106**, 2193–2220.

Li, Y.G. & Leary, P.C., 1990. Fault zone trapped seismic waves, *Bull. seism. Soc. Am.*, **80**, 12 451–12 471.

Li, Z., Zhang, H. & Peng, Z., 2014. Structure-controlled seismic anisotropy along the Karadere-Düzce branch of the North Anatolian Fault revealed by shear-wave splitting tomography, *Earth planet. Sci. Lett.*, **391**, 319–326.

Liu, C., Xu, L. & Chen, Y., 2009. Quick moment tensor solution for 6 April, 2009, L'Aquila, Italy, earthquake, *Earthq. Sci.* **22**, 449–450.

Liu, E. & Crampin, S., 1990. Effects of the internal shear wave window: comparison with anisotropy induced splitting, *J. geophys. Res.*, **95**, 11 275–11 281.

Liu, Y., Crampin, S. & Main, I., 1997. Shear-wave anisotropy: spatial and temporal variations in time delays at Parkfield, central California, *Geophys. J. Int.*, **130**, 771–785.

Liu, Y., Teng, T.-L. & Zion, Ben, Y., 2004. Systematic analysis of shear-wave splitting in the aftershock zone of the 1999 Chi-Chi, Taiwan, earthquake: shallow crustal anisotropy and lack of precursory variations, *Bull. seism. Soc. Am.*, **94**, 2330–2347.

Liu, Y., Teng, T.-L. & Ben Zion, Y., 2005. Near-surface seismic anisotropy, attenuation and dispersion in the aftershock region of the 1999 Chi-Chi earthquake, *Geophys. J. Int.*, **160**, 695–706.

Liu, Y., Zhang, H., Thurber, C. & Roecker, S., 2008. Shear wave anisotropy in the crust around the San Andreas fault near Parkfield: spatial and temporal analysis, *Geophys. J. Int.*, **172**, 957–970.

Lucente, P.F., De Gori, P., Margheriti, L., Piccinini, D., Di Bona, M., Chiarabba, C. & Piana Agostinetti, N., 2010. Temporal variation of seismic velocity and anisotropy before the 2009 Mw6.3 L'Aquila earthquake, Italy, *Geology*, **38**, 1015–1028.

Malinverno, A. & Ryan, W.B.F., 1986. Extension in the Tyrrhenian sea and shortening in the Apennines as result of arc migration driven by sinking of the lithosphere, *Tectonics*, **5**, 227–245.

Mardia, K.V. & Jupp, P.E., 2000. *Directional Statistics*, John Wiley, 429 pp.
Margheriti, L. *et al.*, 2010. Emergenza "L'Aquila2009": la campagna di acquisizione dati della rete sismica mobile stand-alone del Centro Nazionale Terremoti, in *Rapporti Tecnici*, 151 pp., INGV.
Margheriti, L., Ferulano, M.F. & Di Bona, M., 2006. Seismic anisotropy and its relation with crust and stress field in the Reggio Emilia region (Northern Italy), *Geophys. J. Int.*, **167**(2), 1035–1043.
Martin, P., Arroucau, P. & Vlahovic, G., 2014. Shear-wave splitting study of crustal anisotropy in the New Madrid Seismic Zone, *Bull. seism. Soc. Am.*, **194**(3), 1100–1110.
Matharu, G., Bostock, M.G., Christensen, N.I. & Tromp, J., 2014. Crustal anisotropy in a subduction zone forearc: Northern Cascadia, *J. geophys. Res.*, **119**, 7058–7078.
Mizuno, T., Ito, H., Kuwahara, Y., Imanishi, K. & Takeda, T., 2005. Spatial variation of shear-wave splitting across an active fault and its implication for stress accumulation mechanism of inland earthquakes: the Atotsugawa fault case, *Geophys. Res. Lett.*, **32**, L20305, doi:10.1029/2005GL023875.
Montone, P., Mariucci, MT. & Pierdominici, S., 2012. The Italian present-day stress map, *Geophys. J. Int.*, **189**, 705–716.
Mueller, M.C., 1991. Prediction of lateral variability in fracture intensity using multicomponent shear-wave seismic as precursor to horizontal drilling, *Geophys. J. Int.*, **107**, 409–415.
Munson, C.G., Thurber, C.H., Li, Y. & Okubo, P.G., 1995. Crustal shear wave anisotropy in southern Hawaii: spatial and temporal analysis, *J. geophys. Res.*, **100**(B10), 20 367–20 377.
Nur, A. & Simmons, G., 1969. Stress-induced velocity anisotropy in rock—an experimental study, *J. geophys. Res.*, **74**(27), 6667–6674.
Nuttli, O., 1961. The effect of earth's surface on the *S*-wave particle motion, *Bull. seism. Soc. Am.*, **51**, 237–246.
O'Connell, R.J. & Budiansky, B., 1974. Seismic velocities in dry and saturated cracked solids, *J. geophys. Res.*, **79**, 5412–5426.
Padhy, S. & Crampin, S., 2006. High pore-fluid pressures at Bhuj, inferred from 900-flips in shear-wave polarizations, *Geophys. J. Int.*, **164**, 370–376.
Pantosti, D., D'Addezio, G. & Cinti, F.R., 1996. Paleoseismicity of the Ovindoli–Pezza fault, central Apennines, Italy: a history including a large, previously unrecorded earthquake in the middle ages (860–1300 A.D.), *J. geophys. Res.*, **101**, 5937–5959.
Pastori, M., Piccinin, D., Margheriti, L., Improta, L., Valoroso, L., Chiaraluce, L. & Chiarabba, C., 2009. Stress aligned cracks in the upper crust of the Val d'Agri region as revealed by shear wave splitting, *Geophys. J. Int.*, **179**(1), 601–614.
Pastori, M. *et al.*, 2012. Crustal fracturing and presence of fluids as revealed by seismic anisotropy; case histories from seismogenic areas in the Apennines (Italy), *Boll. Geofis. Teor. App.*, **53**(4), 417–433.
Patacca, E., Scandone, P., Di Luzio, E., Cavinato, G. & Parotto, M., 2008. Structural architecture of the central Apennines: interpretation of the CROP 11 seismic profile from the Adriatic coast to the orographic divide, *Tectonics*, **27**, TC3006, doi:10.1029/2005TC001917.
Paulssen, H., 2004. Crustal anisotropy in southern California from local earthquake data, *Geophys. Res. Lett.*, **31**, L01601, doi:10.1029/2003GL018654.
Peng, Z. & Ben-Zion, Y., 2004. Systematic analysis of crustal anisotropy along the Karadere-Duzce branch of the North Anatolian fault, *Geophys. J. Int.*, **159**, 253–272.
Peng, Z. & Ben-Zion, Y., 2005. Spatiotemporal variations of crustal anisotropy from similar events in aftershocks of the 1999 M7.4 Izmit and M7.1 Düzce, Turkey, Earthquake sequences, *Geophys. J. Int.*, **160**, 1027–1043.
Piccinini, D., Margheriti, L., Chiaraluce, L. & Cocco, M., 2006. Space and time variations of crustal anisotropy during the 1997 Umbria-Marche, central Italy, seismic sequence, *Geophys. J. Int.*, **167**, 1482–1490.
Piccinini, D., Pastori, M. & Margheriti, L., 2013. ANISOMAT+: an automatic tool to retrieve seismic anisotropy from local earthquakes, *Comp. Geosci.*, **56**, 62–68.
Pizzi, A. & Galadini, F., 2009. Pre-existing cross-structures and active fault segmentation in the northern-central Apennines (Italy), *Tectonophysics*, **476**, 304–319.
Pizzi, A., Calamita, F., Coltorti, M. & Pieruccini, P., 2002. Quaternary normal faults, intramontane basins and seismicity in the Umbria- Marche-Abruzzi Apennine Ridge (Italy): contribution of neotectonic analysis to seismic hazard assessment, *Boll. Soc. Geol. It.*, **1**, 923–929.
Pondrelli, S., Salimbeni, S., Morelli, A., Ekström, G., Olivieri, M. & Boschi, E., 2010. Seismic moment tensors of the April 2009, L'Aquila (central Italy) earthquake sequence, *Geophys. J. Int.* **180**, 238–242.
Pucci, S. *et al.*, 2014. Quaternary geology of the Middle Aterno Valey, 2009 L'Aquila earthquake area (Abruzzi Apennines, Italy), *J. Maps*, doi:10.1080/17445647.2014.927128.
Rial, J.A., Elkibbi, M. & Yang, M., 2005. Shear-wave splitting as a tool for the characterization of geothermal fractured reservoirs: lessons learned, *Geothermics*, **34**(3), 365–385.
Roberts, G.P. & Michetti, A.M., 2004. Spatial and temporal variations in growth rates along active normal fault systems; an example from the Lazio–Abruzzo Apennines, central Italy, *J. Struct. Geol.*, **26**, 339–376.
Rosenbaum, G., Lister, G.S. & Duboz, C., 2002. Reconstruction of the tectonic evolution of the western Mediterranean since the Oligocene, *J. Virt. Exp.*, **8,** 107–130.
Saiga, A., Hiramatsu, Y., Ooida, T. & Yamaoka, K., 2003. Spatial variation in the crustal anisotropy and its temporal variation associated with the moderate size earthquake in the Tokai region, central Japan, *Geophys. J. Int.*, **154**, 695–705.
Salvi, S., Cinti, F.R., Colini, L., D'Addezio, G., Doumaz, F. & Pettinelli, E., 2003. Investigation of the active Celano-L'Aquila fault system, Abruzzi (Central Apennines, Italy) with combined ground-penetrating radar and paleoseismic trenching, *Geophys. J. Int.*, **155**, 805–818.
Savage, M.K., Peppin, W.A. & Vetter, U.R., 1990. Shear-wave anisotropy and stress direction in and near Long Valley Caldera, California, 1979–1988, *J. geophys. Res.*, **95**, 11 165–11 177.
Savage, M.K., Shih, X.R., Meyer, R.P. & Aster, R.C., 1989. Shear-wave anisotropy of active tectonic regions via automated S-wave polarization analysis, *Tectonophysics*, **165**(1–4), 279–292.
Sayers, C.M., 1994. The elastic anisotropy of shales, *J. geophys. Res.*, **99**, 767–774.
Schlagenhauf, A., Gaudemer, Y., Benedetti, L., Manighetti, I., Palumbo, L., Schimmelpfenning, I., Finkel, R. & Pou, K., 2010. Using *in situ* Chlorine-36 cosmonuclide to recover past earthquake histories on limestone normal fault scarps: a reappraisal of methodology and interpretations, *Geophys. J. Int.*, **182**, 36–72.
Schutt, D., Humphreys, E.D. & Dueker, K., 1998. Anisotropy of the yellowstone hot spot wake, Eastern Snake River Plain, Idaho, *Pure appl. Geophys.*, **151**, 443–462.
Scognamiglio, L., Tinti, E., Michelini, A., Dreger, D.S., Cirella, A., Cocco, M., Mazza, S. & Piatanesi, A., 2010. Fast determination of moment tensors and ruptures history: what has been learned from the 6 April 2009 L'Aquila earthquake sequence, *Seism. Res. Lett.*, **81**, 892–906.
Shi, Y.-T., Gao, Y., Wu, J., Luo, Y. & Su, Y.-J., 2006. Seismic anisotropy of the crust in Yunnan, China: polarizations of fast shear-waves, *Acta Seismol. Sin.* (English Edition), **19**, 620–632.
Sibson, R., 1977. Fault rocks and fault mechanisms, *J. Geol. Soc.*, **133**, 191–213.
Sibson, R., Ghisetti, F. & Ristau, J., 2011. Stress control of an evolving strike-slip fault system during the 2010–2011 Canterbury, New Zealand, earthquake sequence, *Seism. Res. Lett.*, **82**, 824–832.
Syracuse, E. *et al.*, 2012. Temporal and spatial evolution of hypocenters and anisotropy from the Darfield aftershock sequence: implications for fault geometry and age, *N.Z. J. geol. Geophys.*, **55**, 287–293.
Tadokoro, K. *et al.*, 2002. Monitoring of fault healing after the 1999 Kocaeli, Turkey, earthquake, *J. Seismol.*, **6**, 411–417.
Tadokoro, K., Ando, M. & Umeda, Y., 1999. Swave splitting in the aftershock region of the 1995 Hyogo-ken Nanbu earthquake, *J. geophys. Res.*, **104**, 981–991.
Terakawa, T., Zoporowski, A., Galvan, B. & Miller, S.A., 2013. High-pressure fluid at hypocentral depth in the L'Aquila region inferred from earthquake focal mechanisms, *Geology*, **38**, 995–998.

Thomsen, L., 1986. Weak elastic anisotropy: applied seismic anisotropy: theory, background, and field studies, *Geophys. Reprint Ser.*, **20**, 34–46.
Valcke, S.L.A., Casey, M., Lloyd, G.E., Kendall, J-M. & Fisher, Q.J., 2006. Lattice preferred orientation and seismic anisotropy in sedimentary rocks, *Geophys. J. Int.*, **166**, 652–666.
Valoroso, L., Chiaraluce, L., Piccinini, D., Di Stefano, R., Schaff, D. & Waldhauser, F., 2013. Radiography of a normal fault system by 64000 high-precision earthquake locations: the 2009 L'Aquila (central Italy) case study, *J. geophys. Res.*, **118**, 1156–1176.
Verdon, J.P., Angus, D.A., Kendall, J.-M. & Hall, S.A., 2008. The effect of microstructure and nonlinear stress on anisotropic seismic velocities, *Geophysics*, **73**(4), D41–D51.
Vezzani, L. & Ghisetti, F., 1998. *Carta Geologica Dell'Abruzzo, 1:100000*, SELCA.
Villani, F., Tulliani, V., Sapia, V., Fierro, E., Civico, R. & Pantosti, D., 2015a. Shallow subsurface imaging of the Piano di Pezza active normal fault (central Italy) by high-resolution refraction and electrical resistivity tomography coupled with time-domain electromagnetic data, *Geophys. J. Int.*, **203**(3), 1482–1494.
Villani, F. *et al.*, 2015b. Shallow subsurface imaging of the Piano di Pezza active normal fault (Central Italy) by high-resolution refraction and electrical resistivity tomography coupled with time-domain electromagnetic data, in *Abstract Volume 6th International INQUA Meeting on Paleoseismology, Active Tectonics and Archaeoseismology, 19|24 April 2015, Pescina, Fucino Basin, Italy*, Vol. 27, pp. 511–514, eds Blumetti, A.M., Cinti, F.R., De Martini, P.M., Galadini, F., Guerrieri, L., Michetti, A.M., Pantrosti, D. & Vittori, E., Miscellanea, INGV.
Wang, C.Y., 1984. On the constitution of the San Andreas fault zone in central California, *J. geophys. Res.*, **89**, 5558–5866.
Wessel, P. & Smith, W.H.F., 1998. New improved version of the generic mapping tools released, *EOS, Trans. Am. geophys. Un.*, **79**, 579, doi:10.1029/98EO00426.
Wu, J., Gao, Y. & Chen, Y.-T., 2009. Shear-wave splitting in the crust beneath the southeast Capital area of North China, *J. Seismol.*, **13**, 277–286.
Wüstefeld, A. & Bokelmann, G., 2007. Null detection in shear-wave splitting measurements, *Bull. seism. Soc. Am.*, **97**(4), 1204–1211.
Zatsepin, S.V. & Crampin, S., 1997. Modelling the compliance of crustal rock—I. Response of shear-wave splitting to differential stress, *Geophys. J. Int.*, **129**, 477–494.
Zhang, Z. & Schwartz, S.Y., 1994. Seismic anisotropy in the shallow crust of the Loma Prieta segment of the San Andreas fault system, *J. geophys. Res.*, **99**, 9651–9661.
Zinke, J.C. & Zoback, M.D., 2000. Structure-related and stress-induced shear-wave velocity anisotropy: observations from microearthquakes near the Calaveras fault in central California, *Bull. seism. Soc. Am.*, **90**, 1305–1312.

SUPPORTING INFORMATION

Additional Supporting Information may be found in the online version of this paper:

Figure S1. Map of distributions of fast polarization directions. Fast directions φ are displayed as a single measurement for individual station–earthquake pairs and plotted as red solid bars at the midpoint between the source and the stations. Each bar is oriented in the φ direction with length proportional to the corresponding delay time, δt. The results clearly show the high variability of φ and δt. On the map are also shown the main structural lineaments (solid black and dark red lines), the coseismic surface ruptures (green solid traces) and the surface projection of main fault plane (blue box) (for more detail see also Fig. 1).
Figure S2a,b. Equal area projection evaluated as in Fig. 5 but for the other stations that return $\geq$8 good measurements. The stations are ordered moving from NW to SE through the study area.
Figure S3a,b. Plots of individual resampled delay times versus hypocentral depth for the stations with $\geq$8 good measurements. The stations are ordered from NW to SE through the study area.
Table S1. Station name, number of measurements, mean and standard deviation of fast direction and of delay time, path-length normalized delay times and the associated standard deviation and *R*-value evaluated at 23 stations that return $\geq$8 high-quality splitting results.
(http://gji.oxfordjournals.org/lookup/suppl/doi:10.1093/gji/ggv536/-/DC1).

Please note: Oxford University Press is not responsible for the content or functionality of any supporting materials supplied by the authors. Any queries (other than missing material) should be directed to the corresponding author for the paper.